Spectral and hyper eddy viscosity in high-Reynolds-number turbulence

By STEFANO CERUTTI[1], CHARLES MENEVEAU[1,2], AND OMAR M. KNIO[1,2]

[1] Department of Mechanical Engineering,
[2] Center for Environmental and Applied Fluid Mechanics,
The Johns Hopkins University, Baltimore, MD 21218, USA

For the purpose of studying the spectral properties of energy transfer between large and small scales in high-Reynolds-number turbulence, we measure the longitudinal subgrid-scale (SGS) dissipation spectrum, defined as the co-spectrum of the SGS stress and filtered strain-rate tensors. An array of four closely spaced X-wire probes enables us to approximate a two-dimensional box filter by averaging over different probe locations (cross-stream filtering) and in time (streamwise filtering using Taylor's hypothesis). We analyse data taken at the centreline of a cylinder wake at Reynolds numbers up to $R_\lambda \sim 450$. Using the assumption of local isotropy, the longitudinal SGS stress and filtered strain-rate co-spectrum is transformed into a radial co-spectrum, which allows us to evaluate the spectral eddy viscosity, $v(k, k_\Delta)$. In agreement with classical two-point closure predictions, for graded filters, the spectral eddy viscosity deduced from the box-filtered data decreases near the filter wavenumber k_Δ. When using a spectral cutoff filter in the streamwise direction (with a box-filter in the cross-stream direction) a cusp behaviour near the filter scale is observed. In physical space, certain features of a wavenumber-dependent eddy viscosity can be approximated by a combination of a regular and a hyper-viscosity term. A hyper-viscous term is also suggested from considering equilibrium between production and SGS dissipation of resolved enstrophy. Assuming local isotropy, the dimensionless coefficient of the hyper-viscous term can be related to the skewness coefficient of filtered velocity gradients. The skewness is measured from the X-wire array and from direct numerical simulation of isotropic turbulence. The results show that the hyper-viscosity coefficient is negative for graded filters and positive for spectral filters. These trends are in agreement with the spectral eddy viscosity measured directly from the SGS stress–strain rate co-spectrum. The results provide significant support, now at high Reynolds numbers, for the ability of classical two-point closures to predict general trends of mean energy transfer in locally isotropic turbulence.

1. Introduction

In large eddy simulations (LES) of turbulent flows, the effective equations for the large-scale velocity field $\tilde{u}_i$ include the divergence of an additional tensor

$$\tau_{ij} = \widetilde{u_i u_j} - \tilde{u}_i \tilde{u}_j, \tag{1.1}$$

called the subgrid-scale (SGS) stress tensor. The tilde represents a low-pass spatial filtering operation at scale Δ (convolution with some homogeneous kernel $G_\Delta(x)$). The

quantity τ_{ij} must be modelled in terms of the resolved field $\tilde{u}_i$. Existing subgrid models may be grouped into several basic categories: eddy viscosity, stochastic, similarity, and (more recently) assumed SGS velocity models.

The most common approach is based on the eddy-viscosity assumption,

$$\tau_{ij}^d \equiv \tau_{ij} - \tfrac{1}{3}\tau_{kk}\delta_{ij} = -2v_T\tilde{S}_{ij}, \tag{1.2}$$

where τ_{ij}^d is the deviatoric part of τ_{ij} and $\tilde{S}_{ij}$ is the resolved strain-rate tensor. This approach includes a number of variants for evaluating the eddy viscosity v_T. The Smagorinsky model (Smagorinsky 1963), where $v_T = (c_s\varDelta)^2|\tilde{S}|$, is the best-known. Another variant is the so-called kinetic-energy model (Schumann 1975; Mason 1994), where an additional scalar transport equation for the SGS kinetic energy is solved. An important recent development in subgrid modelling is the dynamic procedure (Germano *et al.* 1991; Lilly 1992), where the model coefficient c_s is evaluated from the resolved scales during an LES.

In these formulations, the eddy viscosity acts equally on all scales of motion, i.e. it is a nonlinear, but 'simple' viscosity. However, it has been shown by Kraichnan (1976) that if it is considered in detail how the eddy viscosity acts upon different wavenumber modes, the eddy viscosity must be allowed to depend upon the wavenumber magnitude. Specifically, let $E_<(k,t)$ be the energy spectrum of the filtered velocity field. The quantity $E_<(k,t)$ is defined by

$$E_<(k,t) \equiv |\hat{G}_\varDelta(k)|^2 E(k,t), \tag{1.3}$$

where $\hat{G}_\varDelta(k)$ is the Fourier transform of the filter, and $E(k,t)$ the radial energy spectrum of the turbulence. The quantity $E_<(k,t)$ evolves according to

$$\left(\frac{\partial}{\partial t} + 2vk^2\right)E_<(k,t) = F(k,t) + T_<(k,t) - H(k,t), \tag{1.4}$$

where $F(k,t)$ is the energy injection by large-scale forces, and $T_<(k,t)$ is the transfer spectrum of resolved scales. The quantity $T_<(k,t)$ is typically negative at low wavenumbers (energy is extracted from the large scales) and positive near the filter wavenumber $k_\varDelta = \pi/\varDelta$ (energy is deposited by the resolved nonlinear interactions near the filter scale $\varDelta$). The quantity $H(k,t)$ is the SGS dissipation spectrum, given by

$$H(k,t) = -\sum_{|\boldsymbol{k}|=k}\widehat{\tau}_{ij}(\boldsymbol{k},t)\widehat{\tilde{S}}_{ij}^{*}(\boldsymbol{k},t). \tag{1.5}$$

The symbol $\widehat{(\ )}$ denotes the Fourier transform and $(\ )^*$ the complex conjugate; the summation is over a spherical wavenumber shell of constant radius k. The quantity $H(k,t)$ represents the rate at which energy is transferred from a given wavenumber shell at k into the subgrid scales. Even if the actual momentum transfer associated with τ_{ij} cannot be represented as an eddy viscosity (owing to a lack of scale-separation in turbulence), the corresponding spectral SGS dissipation can be written in eddy-viscosity form according to

$$H(k) = 2v_{\text{re}}(k,k_\varDelta)k^2 E_<(k). \tag{1.6}$$

The quantity $v_{\text{re}}(k,k_\varDelta)$ is the 'real' spectral eddy viscosity, which can always be defined based on the real energy transfer properties of turbulence. Notice that, for notational simplicity, we henceforth omit the time dependence.

The spectral eddy viscosity can be modelled based on classical two-point closures such as TFM (Kraichnan 1976; Herring 1979, 1990) and EDQNM (Leslie & Quarini

1979; Chollet & Lesieur 1981; Chasnov 1991; Lesieur & Métais 1996). These closures predict that $H(k)$ can be written as the sum of two terms: $H_{\mathrm{mod}}(k) = H_{\mathrm{mod}}^+(k) - U_{\mathrm{mod}}(k)$. The first term, $H_{\mathrm{mod}}^+(k)$, is positive and contains a factor equal to $k^2 E_<(k)$, that is to say, it can be written as $H_{\mathrm{mod}}^+(k) = 2v_{\mathrm{mod}}^+(k, k_\Delta) k^2 E_<(k)$. The second term, $-U_{\mathrm{mod}}(k)$, is negative and does not contain a factor proportional to $E_<(k)$. $U(k)$ is commonly referred to as the backscatter spectrum. When both terms ($H_{\mathrm{mod}}^+(k)$ and $-U_{\mathrm{mod}}(k)$) are combined, the resulting 'net' spectral eddy viscosity implied by the closures is simply $v_{\mathrm{mod}}(k, k_\Delta) = v_{\mathrm{mod}}^+(k, k_\Delta) - U_{\mathrm{mod}}(k)[2k^2 E_<(k)]^{-1}$. For a spectral cutoff filter, as $k \to k_\Delta$, the net viscosity $v_{\mathrm{mod}}(k, k_\Delta)$ displays an upward 'cusp', while for low wavenumbers (about $k < 0.3k_\Delta$), $v_{\mathrm{mod}}(k, k_\Delta)$ is essentially equal to a non-zero constant.

For graded filters, such as the Gaussian or the top-hat filter, the EDQNM calculation of Leslie & Quarini (1979) (carried out for the Gaussian filter) shows that the cusp near k_Δ is replaced by a downward trend, i.e. scales near Δ transfer less energy into the SGS range than predicted by a constant eddy viscosity. At low k, again, a non-zero plateau is obtained. The cusp depends also upon details of the low-wavenumber limit of the energy spectrum (Leslie & Quarini 1979; Chollet & Lesieur 1981, see also discussion in McComb 1990, §10.3). The prediction of a cusp for the case of a spectral cutoff filter has been verified in direct numerical simulation (DNS) by Domaradski *et al.* (1987). In these DNS it is observed that $v(k, k_\Delta) \to 0$ at $k \to 0$, without a constant region. This behaviour can be attributed to the low Reynolds numbers of those simulations. More recent results (Langford & Moser 1999) show that at higher Reynolds number (based on DNS with 256^3 modes) the plateau does indeed occur. These authors show that the plateau and cusp behaviour of spectral eddy viscosity for the cutoff filter also arises as the result of an optimization process that minimizes the error between the real stress divergence and linear two-point functionals of resolved velocity. By analysing the results of LES (with a spectral eddy-viscosity model) filtered at a scale well above the numerical resolution (in the inertial range), Métais & Lesieur (1992) obtained also a constant plateau region for the effective spectral viscosity. Renormalization group techniques show that the effects of randomly stirred small scales of fluid motion (Yakhot, Orszag & Yakhot 1989; McComb 1990) can be described, in the limit $k \to 0$ (away from the cutoff scale), by a constant effective viscosity.

As reviewed in Lesieur & Métais (1996), the notion of spectral eddy viscosity can be naturally used in LES of homogeneous flows using the pseudospectral method. A working fit to the theoretical predictions, due to Chollet & Lesieur (1981) and Chollet (1985), is

$$v(k, k_\Delta) = C_K^{-3/2} \left[a_1 + a_2 \exp\left(-3.03 \frac{k_\Delta}{k}\right) \right] \sqrt{\frac{E_<(k_\Delta)}{k_\Delta}} \qquad (a_1 = 0.441, \quad a_2 = 15.3).$$

$$(1.7)$$

This fit has also been used by Briscolini & Santangelo (1994) in LES of homogeneous turbulence. In LES of non-homogeneous flows, which are typically formulated with physical space discretizations such as finite-volume or finite-difference methods, the implementation of a wavenumber-dependent eddy viscosity is not easy. A possible approach is to use hyper viscosity, by including higher-order Laplacians of the velocity as SGS models. For instance, Chollet & Lesieur (1981) argue that the cusp of the spectral eddy viscosity described earlier may be represented in practice with an additional hyper-viscous term of the form $\tau_{ij} \sim -\nabla^4 \tilde{S}_{ij}$. Borue & Orszag (1995, 1998) perform simulations with a hyper-viscous term, to produce an inertial range

that is wider than with regular viscosity. Hyper viscosity has been proposed to damp simulations of two-dimensional flows (see discussion in Lesieur & Métais 1996). A mixed Smagorinsky plus hyper-viscous ($\tau_{ij} \sim \nabla^2 \tilde{S}_{ij}$) model has seen initial applications in conjunction with the dynamic procedure (Dantinne *et al.* 1998).

Thus, considerable theoretical and computational insights into spectral and hyper-viscosity models exist. Unfortunately, so far no experimental measurements have been performed of the SGS dissipation spectrum $H_{\mathrm{re}}(k, t)$, of the spectral eddy viscosity $v_{\mathrm{re}}(k, k_\Delta)$, or of parameters associated with hyper-viscosity terms. Hence, there is a lack of empirical information about these concepts for high-Reynolds-number flows. The main objective of this paper is to present and interpret such direct experimental measurements.

Before giving an outline of this paper, it is important to point out well-known limitations of the basic eddy-viscosity concept, and to give arguments as to why it is still important to continue to study its spectral properties through experiments. As is well known, the lack of scale-separation in turbulent flows violates the central assumption used to justify eddy-viscosity concepts. Not surprisingly then, when the SGS stress tensor τ_{ij} is compared to the filtered strain-rate tensor in individual realizations of the flow in *a priori* tests, the agreement is quite poor (Clark, Ferziger & Reynolds 1979; Bardina, Ferziger & Reynolds 1980; Liu, Meneveau & Katz 1994). A related problem is that eddy-viscosity models do not include backscatter of energy from small to large scales. For this purpose, it has been proposed to add stochastic forcing terms (Leith 1990; Chasnov 1991; Mason & Thomson 1992; Mason 1994; Schumann 1995) to the eddy-viscosity model. Another class of models, the similarity models (Bardina *et al.* 1980; Liu *et al.* 1994) can be motivated by observations of similarity among localized flow phenomena occurring at different scales (Liu *et al.* 1994), and by conditional averaging (Piomelli, Yu & Adrian 1996; O'Neil & Meneveau 1997; Meneveau & Katz 1999). The similarity models also include backscatter. Experience with such models, however, dictates that some eddy-viscosity term must typically be added in order to prevent unphysical solutions and possibly numerical instability. Mixed models (Bardina 1983), consisting of a similarity and an eddy-viscosity term, have been shown to combine the positive features of both approaches (Liu *et al.* 1994). As reviewed in Meneveau & Katz 2000, a growing number of numerical applications using variants of the mixed model provide improved predictions in LES (e.g. Zang *et al.* 1993; Vreman, Geurts & Kuerten 1997; Akhavan *et al.* 2000; Sarghini, Piomelli & Balaras 1999). New-generation SGS closures, that have emerged as alternatives to the eddy-viscosity and similarity models, include the velocity estimation model (Domaradski & Saiki 1997), the fractal model (Scotti & Meneveau 1999) and the vortex model (Misra & Pullin 1997). These models do not assume a specific form for the stress tensor but rather, for the subgrid velocity field.

In any of these new modelling approaches, it is important to understand how energy dissipation acts on different scales of motion. Such understanding can be furthered by measuring the real SGS dissipation spectrum $H_{\mathrm{re}}(k)$ or the real eddy viscosity $v_{\mathrm{re}}(k, k_\Delta)$ and, subsequently, by comparing with SGS dissipation spectra implied by the models. Hence, such measurements are relevant not only in the context of the spectral eddy-viscosity model, but also for other closure approaches. In this paper we present direct measurements of $H_{\mathrm{re}}(k, t)$ and $v_{\mathrm{re}}(k, k_\Delta)$ obtained from hot-wire measurements on the centreline of a turbulent wake behind a cylinder at Reynolds numbers up to $R_\lambda \sim 450$. The focus of this paper is on documenting $H_{\mathrm{re}}(k, t)$ and $v_{\mathrm{re}}(k, k_\Delta)$ for real turbulence at high Reynolds numbers and on comparing with the trends predicted by the classical two-point closures.

In §2 we describe the experimental set-up and briefly review the hot-wire array that permits us to measure signals of the SGS stress and resolved strain-rate tensors. Section 3 presents the main results, consisting of measured SGS dissipation spectra and the corresponding spectral eddy-viscosity distributions. For applications of LES with physical-space discretizations, it is of interest to examine the ability of hyper-viscosity models to reproduce the dissipation characteristics of turbulence. As shown in §4, hyper-viscosity models naturally arise in formulating equilibrium between production and SGS dissipation of resolved enstrophy. There we also show that the skewness factor of the filtered velocity derivative is an important ingredient in the balance between production and SGS dissipation of resolved enstrophy. Measurements of the skewness coefficient are used to quantify the trends of hyper-viscosity terms at high Reynolds number. A discussion of these results and concluding remarks are presented in §5.

2. Instrumentation and experiment in cylinder wake

As outlined in §1, to measure the spectral distribution of SGS dissipation we must measure the SGS stress and filtered strain rate in high-Reynolds-number turbulence. For this purpose, velocity measurements must be spatially filtered. In LES, what is represented on a computational grid are fields filtered in three dimensions. Earlier experimental work (Meneveau 1994; O'Neil & Meneveau 1997) used hot-wire measurements to study variables relevant to SGS modelling and was based on one-dimensional filtering in the streamwise direction (in reality, time filtering using the Taylor hypothesis). While qualitative trends are believed to be captured with the one-dimensional approach, quantitatively more accurate results can be obtained using two-dimensional filtering (see Murray, Piomelli & Wallace (1996) and Tong, Wyngaard & Brasseur (1998) for comparisons of one-dimensional and two-dimensional filtering using numerical data and Porté-Agel *et al.* (2000*a*) using atmospheric field data). Planar particle image velocimetry (PIV) (Liu *et al.* 1994, 1995, 1999; Bastiaans, Rindt & Van Steenhoven 1998) allows the measurement of a two-dimensional velocity field, from which two-dimensional filtered quantities can be evaluated. However, using PIV, the measurement of converged high-order statistics (such as the SGS stress–strain rate co-spectra required here) is challenging owing to present difficulties in accumulating the very long data records needed to achieve statistical convergence. In this work, we use an array of hot wires (Cerutti 1999; Cerutti & Meneveau 2000) which allows us to approximate to a reasonable accuracy a two-dimensional box filter, and to accumulate the long data records needed to achieve statistical convergence.

2.1. *Hot-wire probe array and two-dimensional filtering*

An array of four X-probes has been designed and built in-house to allow us to approximate filtering of data in the direction transverse to the flow (x_2), in addition to time filtering (i.e. filtering in the streamwise (x_1) direction using Taylor's hypothesis). The centres of the four X-probes are positioned $h = 2.286$ mm apart. Each probe is made of a 7.62 cm long, 1.575 mm diameter alumina tube with four 0.406 mm longitudinal holes for the steel prongs, whose centres form a 0.491 mm $\times$ 0.491 mm square. The probe is spot-welded with eight platinum-plated, 2.5 µm diameter tungsten sensor wires. More details about the probe geometry and its construction are presented in Cerutti (1999) and Cerutti & Meneveau (2000). Throughout this paper, the filter size Δ is kept equal to twice the inter-probe distance h, i.e. $\Delta = 2h = 4.58$ mm. Filtering in the x_1 streamwise direction is performed using the trapezoidal rule evaluated on

the successive time samples. The latter are separated by a time f_s^{-1} or a distance $\langle u_1 \rangle f_s^{-1}$, where f_s is the sampling frequency and $\langle u_1 \rangle$ is the mean streamwise velocity.

Filtering over a scale Δ in the x_2-direction involves the signal at four neighbouring points, which are combined to produce a single filtered signal assigned to the geometric centre of the probe. Let $x_2^{(A)}$, $x_2^{(B)}$, $x_2^{(C)}$, and $x_2^{(D)}$ denote the transverse positions of the four probes in the array. The centre position of the probe (i.e. the mid-point between $x_2^{(B)}$ and $x_2^{(C)}$) is denoted by $x_2^{(O)}$. For filtering with a top-hat filter of size $\Delta = 2h$ centred at point $x_2^{(O)}$, we apply the trapezoidal rule to the available points:

$$\tilde{u}_i(x_1, x_2^{(O)}) \simeq \tfrac{1}{16}[u_i(x_1, x_2^{(A)}) + 7\,u_i(x_1, x_2^{(B)}) + 7\,u_i(x_1, x_2^{(C)}) + u_i(x_1, x_2^{(D)})]. \qquad (2.1)$$

The same expression is used to evaluate the filtered product $\widetilde{u_1 u_1}$ needed to evaluate the (longitudinal) SGS stress term τ_{11}. The combination of the x_1 and x_2 filter operations is denoted as the 'array' two-dimensional filter. The quantity $\tilde{S}_{11} = \partial \tilde{u}_1 / \partial x_1$ is evaluated using a finite-difference approximation over a distance equal to the mean streamwise velocity divided by the data acquisition frequency. Other tensor components such as $\partial \tilde{u}_1 / \partial x_2$, $\partial \tilde{u}_2 / \partial x_1$, $\partial \tilde{u}_2 / \partial x_2$, and τ_{12}, τ_{22} can be evaluated (see Cerutti & Meneveau 2000). In the present paper we focus on the longitudinal components since derivatives in the cross-stream direction involve larger errors.

The under-resolution in the cross-stream direction, where only a few points are available, and the additional filtering from the length of the wires generates an error in the array filter as compared to an ideal two-dimensional box filter. In Cerutti & Meneveau (2000), the expected differences between results for an ideal box filter and the discrete array filter are quantified based on an assumed isotropic turbulence spectrum and characteristic lengthscales close to those encountered in the experiments. The results are that the r.m.s. of the $\partial \tilde{u}_1 / \partial x_1$ component differs from the ideal two-dimensional box filter by about 2%, and that the trace of the SGS tensor differs by 5%. We have performed further tests based on earlier two-dimensional PIV data sets in the far field of a turbulent jet (Liu *et al.* 1994). These data have equally good spatial resolution in two directions, with vector spacings at about 5η. We first computed an SGS stress field with a box filter at a scale of 60η (i.e. using 13×13 vectors in each box). Then, a stress field was computed with a 13×4 vector array covering a box of the same size (60η), in which in the x_2-direction only every 4th vector (separated by 20η) was used to mimic the coarse sampling with our array of discrete point sensors. The correlation between the two stress fields was 97%. The r.m.s. of these fields differed by about 3%, which is comparable to the analytical results. When comparing the gradients of the stresses, the correlation was still 95%, indicating very good agreement even at the smallest scales of the stress fields. The good agreement is due to the fact that the SGS stress is dominated by the largest of the unresolved scales. We conclude that the array of sensors gives a sufficiently good representation of a two-dimensional box filter for the purposes of the present study. It is stressed that the good agreement applies to a box filter. For filters with wider spatial support such as the spectral cutoff filter, many more measurement points would probably be needed.

An eight-channel, constant-temperature hot-wire anemometer system (TSI IFA-300) is used to drive the probe in all the experiments. Each X-wire in the array is calibrated using an external compressed air calibrator stage (TSI 1128A) including a specially designed 25 mm diameter round nozzle. By varying the exit speed between 0 and $27\,\mathrm{m\,s^{-1}}$, and the angle of the array in a range between $-30°$ and $30°$, the calibration is performed separately for each X-wire probe in the array. A fourth-order calibration polynomial (Oster & Wygnanski 1982) is fitted to each set of

Data set	Average $\bar{u}_1$ (m s^{-1})	r.m.s. u'_1 (m s^{-1})	r.m.s. u'_2 (m s^{-1})	ℓ (cm)	ε (m^2 s^{-3})	R_λ	η (10^{-4} m)	$\varDelta/\eta$
10V	11.2	0.780	0.652	19.8	4.60	289	1.60	28.5
15V	15.6	1.07	0.898	18.8	11.6	342	1.27	35.9
20V	20.1	1.38	1.16	18.5	23.4	400	1.07	42.8
25V	24.5	1.67	1.41	18.3	40.3	447	0.933	49.0

TABLE 1. Data sets for the cylinder experiment. All data sets consist of 10.5 million points per channel, except for 20V which has 51.4 million each. The characteristic values in this table are obtained by averaging over the four X-wire readings.

measurements. In calibration tests described in Cerutti (1999), it is found that the r.m.s. of the errors between the measured and real velocities over the calibration domain is typically about 0.3% of the velocity, or about 5% of the r.m.s. of turbulent velocities. While not negligible, these calibration errors are strongly correlated from one sample to another and, hence, do not significantly affect longitudinal velocity derivatives and SGS stresses.

2.2. *Experimental conditions and data characterization*

Experiments are performed in the Corrsin wind tunnel, whose test-section is 10 m long and cross-section is 1 m × 1.3 m. A 5.08 cm diameter smooth circular cylinder is placed horizontally, 51 cm downstream of the final 1.27 : 1 contraction at the entrance of the test section. The probe array is placed 3.05 m downstream of the cylinder, i.e. at $x/D = 60$. The line joining the probes of the array (the x_2-direction) is perpendicular to the cylinder axis, so that x_2 is the cross-wake direction. The probe is located at the height of the centreline of the cylinder, to an accuracy of ±1 mm. A Pitot probe installed upstream of the cylinder provides a velocity measurement of the undisturbed flow, prior to interaction with the cylinder. A temperature signal from a thermocouple placed alongside the probe array is used to correct the probe voltages for temperature changes (Cerutti 1999).

To provide some variation in Reynolds number, data sets are acquired for several average free-stream velocities: 10, 15, 20 and 25 m s^{-1}. About 10.5 million points per channel are acquired, except for the 20 m s^{-1} data set, for which we accumulate 51.4 million points per channel. The acquisition frequency is 50 kHz for all data sets, with a low-pass filter at 20 kHz. Table 1 contains the parameters of each experimental data set.

The longitudinal integral scale, ℓ, is calculated using Taylor's hypothesis and by integrating the u_1 autocorrelation function from the origin to the first zero crossing (FZC). Since the viscous range is not fully resolved in our measurements, an estimate for the energy dissipation rate ε is obtained from the third-order structure function. However, at present Reynolds numbers, the asymptotic scaling of the $\frac{4}{5}$th law is not achieved owing to large-scale effects (forcing or spatial non-homogeneity). Following the procedure proposed by Lindborg (1999), such effects are taken into account by using his equation (6); we find, however, that the standard value $C_{\epsilon_2} = 1.92$ provides a better fit to our results. Values of ϵ obtained in this fashion (typically 15–20% higher than without the Lindborg (1999) correction) are listed in Table 1. The Taylor-scale Reynolds number $R_\lambda = u'_1 \lambda / \nu$ is calculated using $\lambda^2 = 15 \nu u'^2_1 / \varepsilon$, and the Kolmogorov scale η is evaluated according to $\eta = \left(\nu^3 / \varepsilon \right)^{1/4}$.
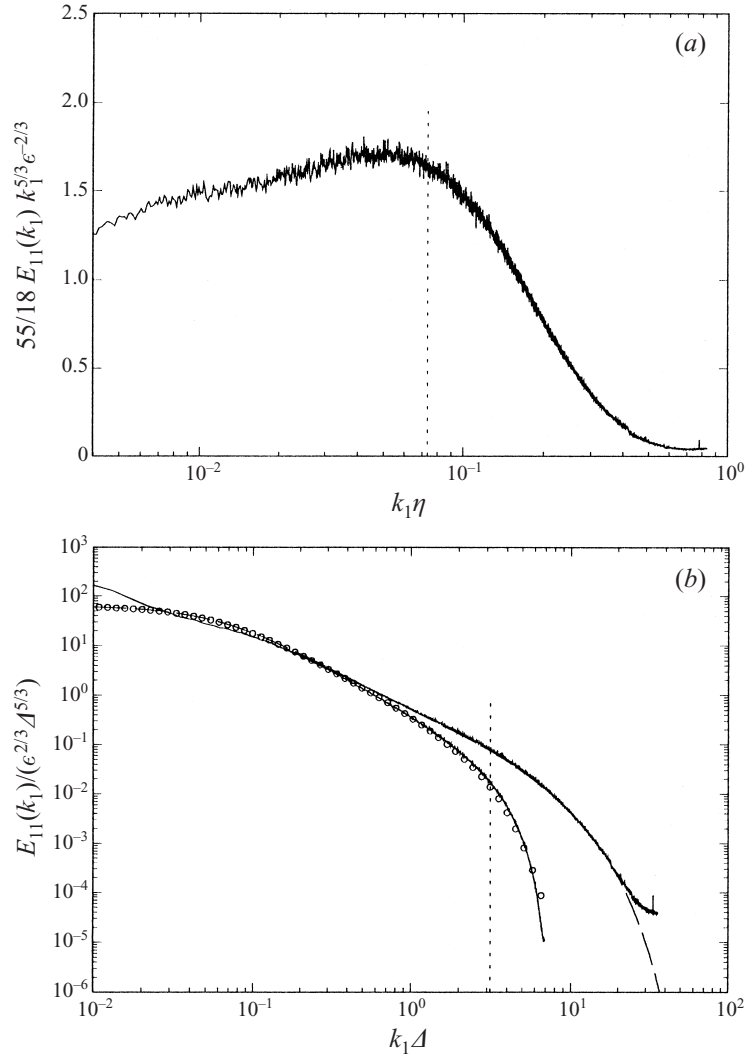
FIGURE 1. Longitudinal energy spectra in the cylinder wake at $R_\lambda \sim 400$ (20V data set). (*a*) Solid line: premultiplied spectrum. Vertical dotted line: filter wavenumber π/Δ. (*b*) Filtered and unfiltered spectra. Upper solid line: spectrum of unfiltered data. Lower solid line: spectrum of array filtered data. Long-dashed line: fit to the unfiltered spectrum. Vertical dotted line: filter wavenumber k_Δ. Circles: longitudinal spectrum obtained from the radial spectrum of unfiltered velocity, multiplied by the transfer function of a radially symmetric top-hat filter in Fourier space.

Longitudinal energy spectra of unfiltered and filtered velocity signals are computed by dividing total records into about 640 segments (3136 segments for the 20V data) of 16 384 points each. The segments are windowed using a Bartlett window. Figure 1(*a*) shows the resulting spectrum for the 20V data set, premultiplied by $\frac{55}{18}\epsilon^{-2/3}k^{5/3}$. Also shown as a dotted line is the filter wavenumber π/Δ which falls towards the end of the inertial range, in the 'bottleneck' part of the spectrum, close to the beginning of the transition to the viscous range.

In Cerutti & Meneveau (2000), a detailed comparison of the effects of filtering in the x_1- and x_2-directions is presented. For completeness, in figure 1(*b*) we present
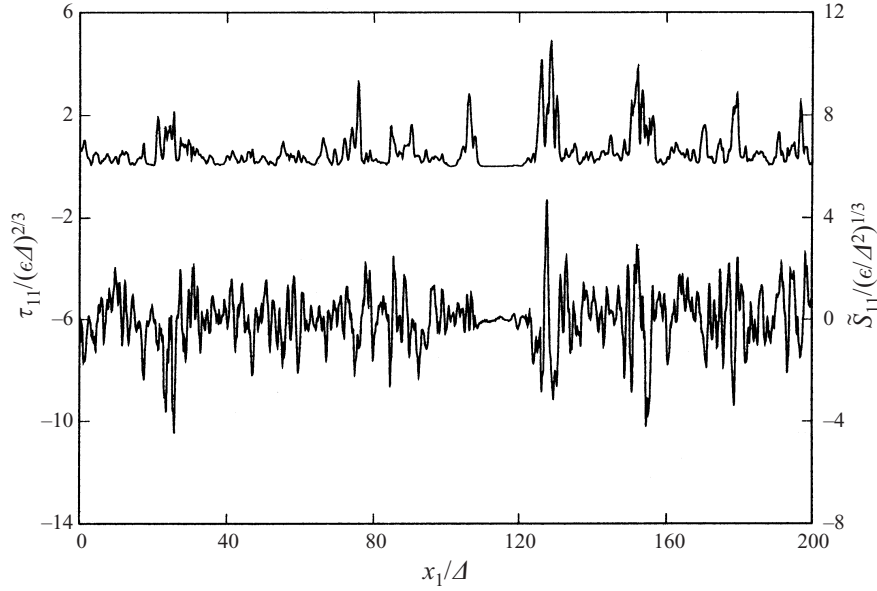
FIGURE 2. Typical segment of SGS stress (τ_{11}, top curve, left-hand scale) and strain-rate signals ($\tilde{S}_{11}$ bottom curve, right-hand scale), evaluated from the experimental measurements in the cylinder wake (data set 25V) at $R_\lambda \sim 450$, using the four-probe array.

the longitudinal spectra of unfiltered and filtered streamwise velocity, plotted in non-dimensional units, using scaling with the filter size. The dotted line at $k_1 \Delta = \pi$ shows the filter wavenumber $k_\Delta \equiv \pi/\Delta$, with $\Delta = 4.58$ mm. As expected, the array filter eliminates much of the kinetic energy at small scales. To quantify how closely the two-dimensional array filter approximates a true three-dimensional top-hat filter, the longitudinal spectrum of the streamwise velocity filtered in three-dimensions using a radially symmetric box filter is shown in figure 1(b) as circles. These data are obtained by assuming local isotropy and evaluating, from the longitudinal spectrum of unfiltered velocity $E_{11}(k_1)$, the corresponding radial three-dimensional spectrum $E(k)$ using the classical relationship between one-dimensional and three-dimensional spectra (Batchelor 1953; Monin & Yaglom 1971). This radial spectrum is based on a smooth fit whose one-dimensional transform agrees with the data, as shown in figure 1 (long-dashed line). The radial spectrum is then multiplied by the transfer function of a radial top-hat (box) filter and transformed back into a longitudinal spectrum (for details see Cerutti & Meneveau 2000). As can be seen by comparing the circles in figure 1(b) with the spectrum of array-filtered velocity (the lower solid curve), the latter provides a good approximation for the former, except for a slight over-prediction near the grid scale. Since the two-dimensional array filter eliminates less energy than the full three-dimensional filter, an over-prediction is to be expected. This comparison indicates that the array filter provides a good approximation of the three-dimensional radial filter as far as longitudinal spectra in the x_1-direction is concerned.

3. SGS dissipation spectrum and spectral eddy viscosity

Our goal is to measure the radial SGS dissipation spectrum $H(k)$, defined in equation (1.5) in terms of a shell sum in three-dimensional Fourier space. From the
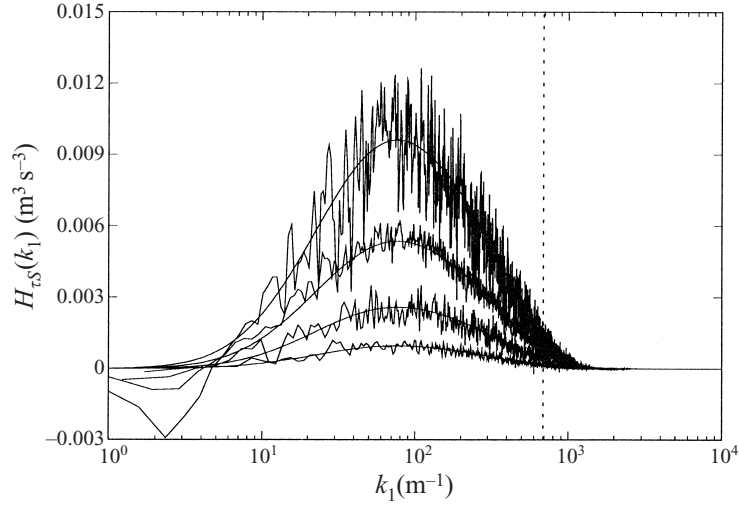
FIGURE 3. Longitudinal co-spectra $H_{\tau S}(k_1)$ of τ_{11} and $\tilde{S}_{11}$ for the various data sets. From lower to upper line: 10V, 15V, 20V, and 25V. Significant scatter remains in the data, even after averaging over 10.5 million points for the 10V, 15V, and 25V, and over 51.4 million samples for the 20V data set. Superimposed on the co-spectra are the fits used to compute the spectral eddy-viscosity. Vertical dotted line: $k_\Delta = \pi/\Delta \approx 686\,\mathrm{m}^{-1}$.

experiments outlined in the preceding section, we have signals of filtered velocity $\tilde{u}_1$ (and therefore of filtered strain rate $\tilde{S}_{11}$ by taking the streamwise (time) derivative), and of SGS stress τ_{11}. Figure 2 displays a typical segment of both signals. As found previously from one-dimensional signals (Meneveau 1994) and three-dimensional DNS (Cerutti & Meneveau 1998), these variables display strong intermittency, but low correlation in detail. Note, however, that the full tensor element τ_{11} is plotted and not τ_{11}^d since we do not measure the trace. Hence, it is non-negative everywhere. Figure 3 shows the longitudinal co-spectrum $H_{\tau S}(k_1)$ of τ_{11} and $\tilde{S}_{11}$ for the various data sets (10V–25V) in dimensional form. $H_{\tau S}(k_1)$ is defined as

$$H_{\tau S}(k_1) = -2\langle \hat{\tau}_{11}(k_1)\hat{\tilde{S}}^{*}(k_1)\rangle = \frac{1}{\pi}\int_{-\infty}^{\infty} B_{\tau S}(r)\,\mathrm{e}^{-ik_1 r}\,\mathrm{d}r, \tag{3.1}$$

where $\hat{\tau}_{11}(k_1)$ and $\hat{\tilde{S}}^{*}(k_1)$ are the longitudinal Fourier transforms of the SGS stress and strain-rate signals, respectively, and $B_{\tau S}(r)$ is the (negative) stress strain-rate correlation function

$$B_{\tau S}(r) \equiv -\langle \tau_{11}(x)\,\tilde{S}_{11}(x + re_1)\rangle. \tag{3.2}$$

Above, e_1 is a unit vector in the x_1-direction. With the normalization used, the following applies:

$$\int_0^{\infty} H_{\tau S}(k_1)\,\mathrm{d}k_1 = -\langle \tau_{11}\tilde{S}_{11}\rangle.$$

In practice, $H_{\tau S}(k_1)$ is computed from the Fourier transforms of $\tau_{11}(x_1)$ and $\tilde{S}_{11}(x_1)$ using standard FFT on 642 segments (3136 in the 20V case) containing 16 384 points each, and using a Bartlett windowing function. As can be seen in figure 3, $H_{\tau S}(k)$ peaks at about a tenth of the filter wavenumber. This is about the same ratio of scales as occurs between the peak of the molecular dissipation spectrum $(2\nu k^2 E(k))$ and the Kolmogorov wavenumber. Also, note that the peak occurs at nearly the

same wavenumber for all Reynolds numbers. This trend is to be expected since Δ/ℓ remains approximately constant among the data set, and only Δ/η changes.

The integral $\int_0^\infty H_{\tau S}(k_1)\,dk_1$, evaluated using the trapezoidal rule on the measured co-spectrum, is equal to 0.3658, 0.9612, 2.061, and 3.522 m^2 s^{-3} for the 10V, 15V, 20V, and 25V data sets, respectively. We also evaluate $-\langle \tau_{11}\tilde{S}_{11}\rangle$ directly from the data in physical space, obtaining 0.3706, 0.9594, 2.065, and 3.534 m^2 s^{-3}, respectively. The small discrepancies with the integral of the co-spectra (typically less than half a per cent) are due to windowing effects. Assuming SGS isotropy (see the next section for a discussion of the validity of this assumption in this flow), $\langle \tau_{ij}\tilde{S}_{ij}\rangle = \frac{15}{2}\langle \tau_{11}\tilde{S}_{11}\rangle$ (O'Neil & Meneveau 1997). Hence, the total SGS dissipations implied by the longitudinal co-spectra are 2.74, 7.21, 15.5, and 26.4 m^2 s^{-3}, respectively. Comparing with the molecular dissipation ϵ listed in table 1, the present results for the SGS dissipation are smaller than ϵ, by about 35%. The difference may be caused by the fact that molecular viscosity also contributes weakly to energy dissipation, and that conditions of full equilibrium do not apply to the present shear flow.

3.1. *Isotropy relations for SGS dissipation co-spectrum*

Since only longitudinal spectra are available from the present data, we must rely on the assumption of local isotropy in order to relate longitudinal spectra to radial spectra. This assumption is not strictly valid for our data. In a shear flow, small-scale isotropy may be expected only asymptotically at very high Reynolds numbers, when $\Delta \ll \ell$ (although on the wake centreline the effects of mean shear may be minimized). Also, the two-dimensional filtering introduces some anisotropy in the filtered and SGS field, even if the unfiltered fields themselves are isotropic (Kaltenbach 1997). The comparisons of array-filtered and three-dimensional filtered spectra in the previous section suggest that isotropy relations may still hold with sufficient accuracy in the current data.

For energy spectra and third-order velocity correlation functions, the relevant expressions can be found in the literature (e.g. Batchelor 1953). Here, we require expressions for the co-spectrum of SGS stress with resolved strain-rate tensor. While they are of similar form to the two-point third-order velocity correlation function, a summary of the relevant transformations is presented below for completeness.

The radial SGS dissipation spectrum is related to the stress–strain-rate correlation function according to

$$\frac{H(k,t)}{4\pi k^2} = -\langle \hat{\tau}_{ij}(\boldsymbol{k})\hat{\tilde{S}}^*_{ij}(\boldsymbol{k})\rangle = -\frac{1}{8\pi^3}\int \langle \tau_{ij}(\boldsymbol{x})\tilde{S}_{ij}(\boldsymbol{x}+\boldsymbol{r})\rangle\,\mathrm{e}^{-\mathrm{i}\boldsymbol{k}\cdot\boldsymbol{r}}\,\mathrm{d}^3\boldsymbol{r}$$

$$= -\frac{1}{2\pi^2 k}\int_0^\infty \langle \tau_{ij}(\boldsymbol{x})\tilde{S}_{ij}(\boldsymbol{x}+\boldsymbol{r})\rangle r\sin(kr)\,\mathrm{d}r, \qquad (3.3)$$

where the last equality uses the assumption that $\langle \tau_{ij}(\boldsymbol{x})\tilde{S}_{ij}(\boldsymbol{x}+\boldsymbol{r})\rangle$ depends only on $r = |\boldsymbol{r}|$. Under the assumption of local isotropy, this function can be related to the correlation function of the longitudinal stress with the filtered velocity,

$$B_{\tau u}(r) \equiv \langle \tau_{11}(\boldsymbol{x})\tilde{u}_1(\boldsymbol{x}+r\boldsymbol{e}_1)\rangle \qquad (3.4)$$

according to

$$\langle \tau_{ij}(\boldsymbol{x})\tilde{S}_{ij}(\boldsymbol{x}+\boldsymbol{r})\rangle = \frac{7}{2}\frac{\mathrm{d}B_{\tau u}}{\mathrm{d}r} + 4\frac{B_{\tau u}}{r} + \frac{r}{2}\frac{\mathrm{d}^2 B_{\tau u}}{\mathrm{d}r^2}. \qquad (3.5)$$

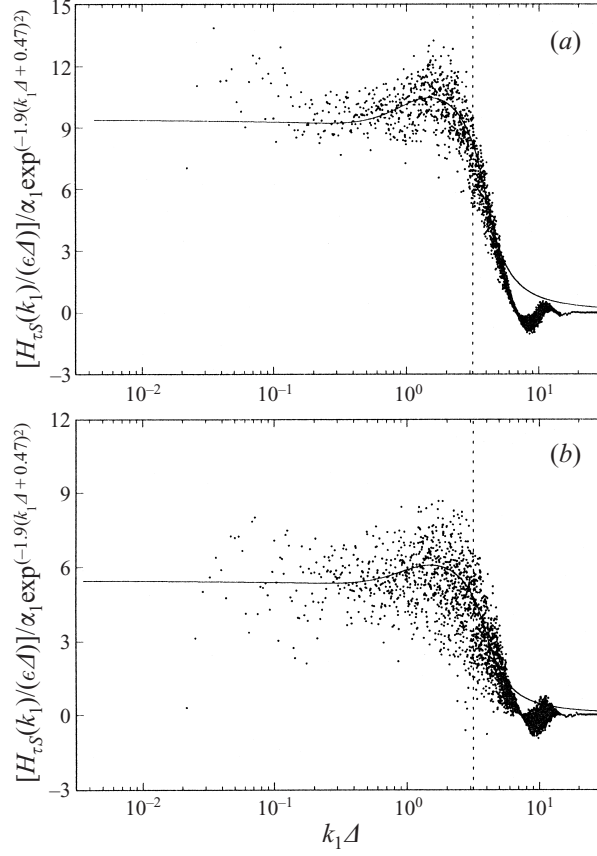This expression is obtained by writing the isotropic form of the third-rank tensor,

FIGURE 4 (a, b). For caption see facing page.

expressed as $\langle \tau_{ij}(\mathbf{x})\tilde{u}_k(\mathbf{x}+\mathbf{r})\rangle$, duly simplified using the divergence-free property of $\tilde{u}_k$ and the symmetry in $i - j$, taking the gradient with respect to $\mathbf{r}$, and performing the required contraction.

Since $H_{\tau S}(k_1) = -2ik_1\hat{B}_{\tau u}$, we have

$$H_{\tau S}(k_1) = -\frac{2k_1}{\pi}\int_0^\infty B_{\tau u}(r)\sin(k_1 r)\,\mathrm{d}r. \tag{3.6}$$

Finally, we substitute equation (3.5) into equation (3.3), and integrate by parts using the fact that $B_{\tau u}(r)$ is an odd function with an r^3 behaviour near the origin (Meneveau 1994). Also, it is assumed that $B_{\tau u}(r)$ decays to zero fast enough as $r \to \infty$. After using equation (3.6), we arrive at

$$H(k) = 4H_{\tau S}(k) - \tfrac{5}{2}k\frac{\mathrm{d}H_{\tau S}}{\mathrm{d}k} + \tfrac{1}{2}k^2\frac{\mathrm{d}^2 H_{\tau S}}{\mathrm{d}k^2} \tag{3.7}$$

which allows us to transform the measurable longitudinal stress–strain-rate co-spectrum $H_{\tau S}(k_1)$ into the radial SGS dissipation spectrum $H(k)$.

Notice that since $\tfrac{1}{3}\delta_{ij}\langle\hat{\tau}_{kk}(\mathbf{k})\hat{\tilde{S}}_{ij}^*(\mathbf{k})\rangle = 0$ (due to incompressibility), the final radial result does not depend on whether the trace is subtracted from τ_{ij} or not. Isotropy conditions relating longitudinal co-spectra to radial ones can be applied to either
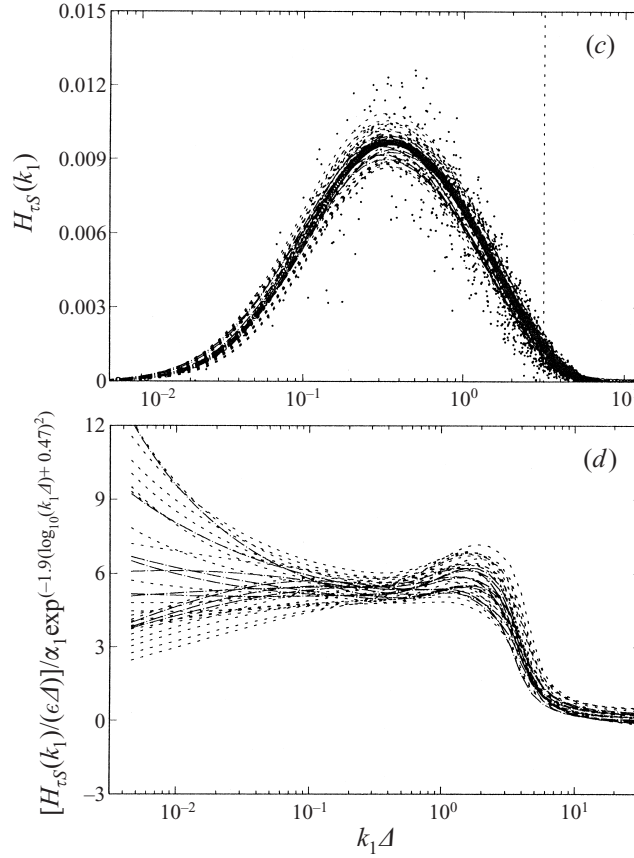
FIGURE 4. Longitudinal co-spectrum $H_{\tau S}(k_1)$ for the (*a*) 20V and (*b*) 25V data sets (shown as scattered dots) and the fit of equation (3.8) (solid line). Both are divided by the factor $\alpha_1 \exp[-1.9(\log_{10}(k_1\varDelta + 0.47)^2]$ so as to highlight details of the important region near the filter wavenumber $k_\varDelta$, indicated by the vertical dotted line. (*c*) Sensitivity analysis with respect to fitting parameters. Dots: original data for 25V. Long and short dashed lines: 32 different functions (equation (3.8)) using 32 sets of parameters. In each set, each of the 9 parameters involved in the fit is chosen randomly within 10% of its baseline value. The long dashes are characterized by a weighted quadratic error below 2×10^{-6}, short dashes have a larger error. (*d*) The same 32 fits of part (*c*) divided by the exponential factor used in part (*a*).

$\langle\hat{\tau}_{ij}\hat{\tilde{S}}^*_{ij}\rangle(k)$ or $\langle\hat{\tau}^d_{ij}\hat{\tilde{S}}^*_{ij}\rangle(k)$, leading to the same result for the final contraction. However, the longitudinal spectrum $\langle\hat{\tau}_{11}\hat{\tilde{S}}_{11}\rangle(k_1)$ that includes the trace need not be the same as $\langle\hat{\tau}^d_{11}\hat{\tilde{S}}_{11}\rangle(k_1)$, where the trace has been subtracted from the SGS stress.

3.2. *Radial SGS dissipation co-spectrum*

In order to apply equation (3.7), the function $H_{\tau S}(k_1)$ must be differentiated twice. For this purpose, a smooth function is fitted through the measurements. The functional form chosen is in the form

$$
\begin{aligned}
H^{\text{fit}}_{\tau S}(k_1)/\varepsilon\varDelta = {} & \alpha_1 \exp[-1.9(\log_{10}(k_1\varDelta) + 0.47)^2] \\
& \times [0.5 - 0.33 \arctan [8.5(\log_{10}(k_1\varDelta) - 0.6)] \\
& + 0.2 \exp[-6(\log_{10}(k_1\varDelta) - 0.26)^2]],
\end{aligned} \tag{3.8}
$$

where the first exponential takes care of the principal functional variation, the arctangent mimics the transition to zero as the grid size is traversed (see figure 4a, b), and the final exponential takes into account the little hump right before the grid wavenumber. The parameters for the four data sets at different velocities are chosen to be equal, except the α terms which are quite close: for 10V, $\alpha_1 = 0.046$; for 15V, $\alpha_1 = 0.049$; for 20V, $\alpha_1 = 0.050$; and for 25V, $\alpha_1 = 0.053$. Figures 4(a) and 4(b) show the data and the fit for the 20V and 25V data sets, divided by $\alpha_1 \exp[-1.9(\log_{10}(k_1 \Delta) + 0.47)^2]$ so as to highlight the most relevant region near the filter scale. Good agreement is observed, except for some oscillations at high wavenumbers. This discrepancy is irrelevant to our discussion, since the oscillations occur at wavenumbers significantly above the filter wavenumber k_Δ. The smooth solid lines in figure 3 show the four fits superimposed on the raw co-spectra.

Since the numerical parameters appearing in equation (3.8) are chosen by visual inspection, a detailed description of the sensitivity of the fit to the choice of parameters is performed. Results are shown in figures 4(c) and 4(d). They show a set of 32 curves (dashed lines) generated with equation (3.8), with the 9 numerical parameters perturbed randomly around their baseline values. Specifically, 32 different sets of 9 parameters are generated. In each set, each of the 9 parameters is chosen randomly with uniform distribution within a range of $\pm 10\%$ of the coefficient's baseline value that appears in equation (3.8). Each parameter is chosen independently from the others. As can be seen in figure 4(c), the baseline case provides a good fit but, typically, a 10% change in the parameters produces somewhat poorer fits. In order to quantify the quality of the fits, the weighted least-squares error

$$\mathscr{E}^2 = \sum_n \frac{[H_{\tau S}(k_n) - F(k_n)]^2}{k_n} \bigg/ \sum_n \frac{1}{k_n}$$

is evaluated, where $H_{\tau S}(k_n)$ are all the data points, and $F(k_n)$ the corresponding fit. The term $1/k_n$ corresponds to a logarithmic spacing of wavenumbers. Out of the 32 random fits, the baseline case has the smallest $\mathscr{E}^2$ ($\mathscr{E}^2 = 1.89 \times 10^{-6}$). We divide, arbitrarily, the fits into two categories: (i) better, defined as those with $\mathscr{E}^2 < 2 \times 10^{-6}$ and shown as long-dashed lines, and (ii) worse, defined as those with $\mathscr{E}^2 > 2 \times 10^{-6}$ and shown as short dashed lines (the worst has $\mathscr{E}^2 = 3.05 \times 10^{-6}$). When plotted in premultiplied fashion in figure 4(d), it can be seen that the better fits remain very close to the baseline case for $k_1 \Delta > 0.1$, but may differ significantly from the baseline case at lower k_1. We conclude that the proposed baseline fit is quite robust to parameters down to about $k_1 \Delta \sim 0.1$, but becomes questionable at lower wavenumbers. At any rate, as is visible in figures 4(a) and 4(b), the scatter in the data is very strong there. In addition to the sensitivity to the fit, there is experimental error. We recall that our error estimate for r.m.s. velocity is about 5% (stemming mostly from calibration uncertainty, see Cerutti & Meneveau 2000). Since the dissipation spectrum is a third-order moment of velocity, we estimate the error level at about $\pm 3 \times 5 = \pm 15\%$. It is not shown in figure 4 since it is smaller than the sensitivity to parameters of the fits, but this error level should also be kept in mind.

Figure 5 shows the radial co-spectrum $H_{re}(k)$ for the four data sets, obtained from applying equation (3.7) to the fits through the longitudinal co-spectra. The peak is now closer to the filter wavenumber (at about two octaves). The level of sensitivity to parameter fits and experimental error is similar to that of the data shown in figure 4.

In order to compute the spectral eddy-viscosity, we also require the radial energy spectrum of filtered velocity. As in Cerutti & Meneveau (2000), the following
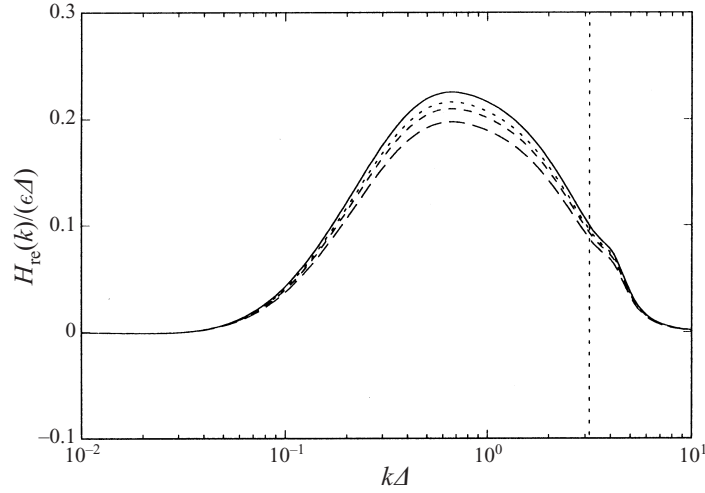
FIGURE 5. Radial co-spectrum $H_{re}(k)$ obtained from the fitted longitudinal co-spectrum, assuming isotropy. Solid line: 25V; dotted line: 20V; short-dashed line: 15V; long-dashed line: 10V. Values are normalized with ϵ and $\varDelta$. The vertical dotted line is the value π. The level of sensitivity to parameters (not shown) is similar to that in figure 4(*c*).

expression for the radial spectrum is used:

$$E_<(k) = \beta_1 \varepsilon^{2/3} k^{-5/3} \left(\frac{k\ell}{\sqrt{k^2 \ell^2 + \beta_2}} \right)^{11/3} e^{-\beta_3 (k\varDelta)^4}, \qquad (3.9)$$

with $\beta_1 = 1.5$, $\beta_2 = 10$ for all spectra, and $\beta_3 = 1.7 \times 10^{-3}$, 1.5×10^{-3}, 1.3×10^{-3}, or 1.0×10^{-3} for the data sets 10V, 15V, 20V, and 25V, respectively. The accuracy of this fit is verified by transforming equation (3.9) to a longitudinal direction and comparing (visually) the result with the measured longitudinal spectrum of $\tilde{u}_1$ (Cerutti & Meneveau 2000).

Figure 6(*a*) shows the resulting spectral eddy-viscosity distributions for the four data sets. Results are normalized with the inertial-range scaling of viscosity, $\epsilon^{1/3} \varDelta^{4/3}$. We have also added error bars which are based on the estimate of $\pm 15\%$ error for third-order moments. Figure 6(*b*) displays the sensitivity of the result to 10% random variations on the parameters used for the fit to the measured co-spectrum (see figure 4*c*).

Within the scatter associated with parameter sensitivity and experimental error, the results suggest a plateau behaviour in the range $0.06 < k\varDelta < 0.7$. Within the overall plateau behaviour, some weak variations may be discerned (although they fall below the scatter): there is a small peak at $k\varDelta \approx 0.4$, before decreasing at higher wavenumbers. However, we recall that at $k\varDelta < 0.1$ the fits become more questionable. As the high-wavenumber limit $k\varDelta \sim \pi$ is approached, the spectral eddy-viscosity decreases to almost zero. Such a decreasing trend was also predicted for the Gaussian filter from the EDQNM analysis of Leslie & Quarini (1979) (squares). While they do not report the analysis for a box filter, they argue that in many important respects the box filter and the Gaussian filter are similar. Their curve (squares with long dashes in figure 6*a*) falls above the present measurements since the figure is scaled to give the total SGS dissipation equal to ϵ, whereas the measured total SGS dissipation is lower. The squares and dot-dashed line represent the EDQNM prediction of Leslie

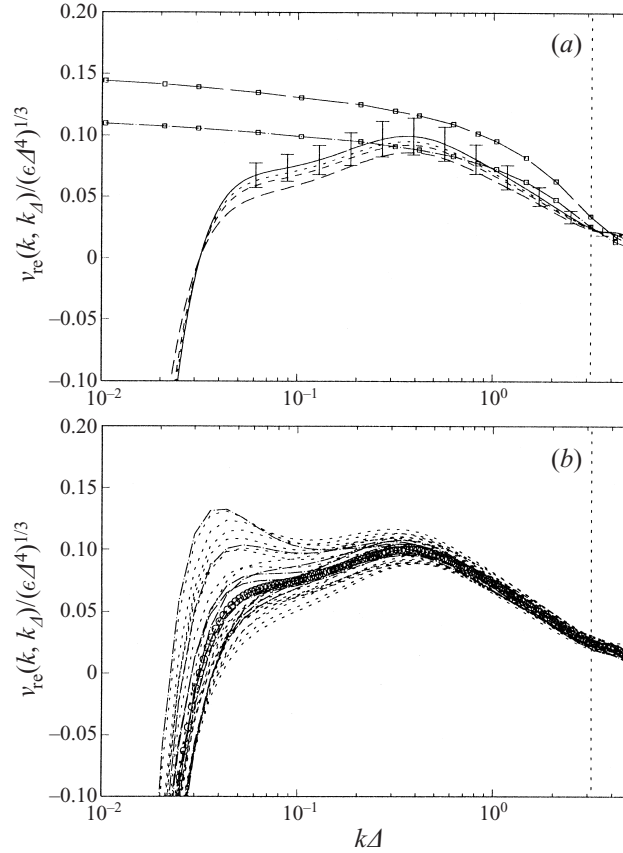FIGURE 6. Spectral eddy-viscosity distributions normalized with $\epsilon^{1/3}\Delta^{4/3}$, obtained from dividing the measured radial co-spectra by $2k^2E_<(k)$. (*a*) Solid line: 25V; dotted line: 20V; short-dashed line: 15V; long-dashed line: 10V. The vertical dotted line is the value π. Error bars (shown only for the 25V case) reflect the expected $\pm15\%$ error level associated with calibration uncertainty (it applies also to the other 3 data sets). Squares: Predictions from EDQNM theory (as read off figure 3 of Leslie & Quarini 1979) for the Gaussian filter. The upper curve (squares and long dashes) is the original prediction. In the lower one (squares and dot-dashed line) the EDQNM result is rescaled so that the integral of $2\nu k^2 E_<$ equals our measured SGS dissipation instead of the molecular dissipation, ϵ. (*b*) Sensitivity to varying randomly the parameters used in equation (3.8). Circles show the baseline case (for the 25V data). The 32 long and short dashed lines correspond to the same lines of figures 4(*c*) and 4(*d*).

& Quarini (1979) but rescaled so as to give the measured SGS dissipation. Taken together with the sensitivity to fitting parameters and experimental error, we conclude that the experimental results agree well with the EDQNM calculation.

The low-wavenumber limit of the approximate plateau behaviour corresponds to $k\ell \sim \frac{1}{2}\pi$, i.e. the non-zero eddy viscosity extends to lengthscales of the order of the integral scale ℓ (slighly larger, in fact). Interestingly, at even lower wavenumbers, there is a region where $H_{re}(k)$ (and hence $\nu_{re}(k,k_\Delta)$) is negative. This trend corresponds to backscatter of energy from the SGS scales towards the very largest scales of the flow from distant interactions, as also observed in low-Reynolds-number DNS (Domaradski *et al.* 1987). However, the negative region of $H_{re}(k)$ must be interpreted with caution since at low k the assumption of isotropy used to infer $H_{re}(k)$ from $H_{\tau S}(k_1)$ does not hold in this shear flow. Still, some support to the notion of backscatter via
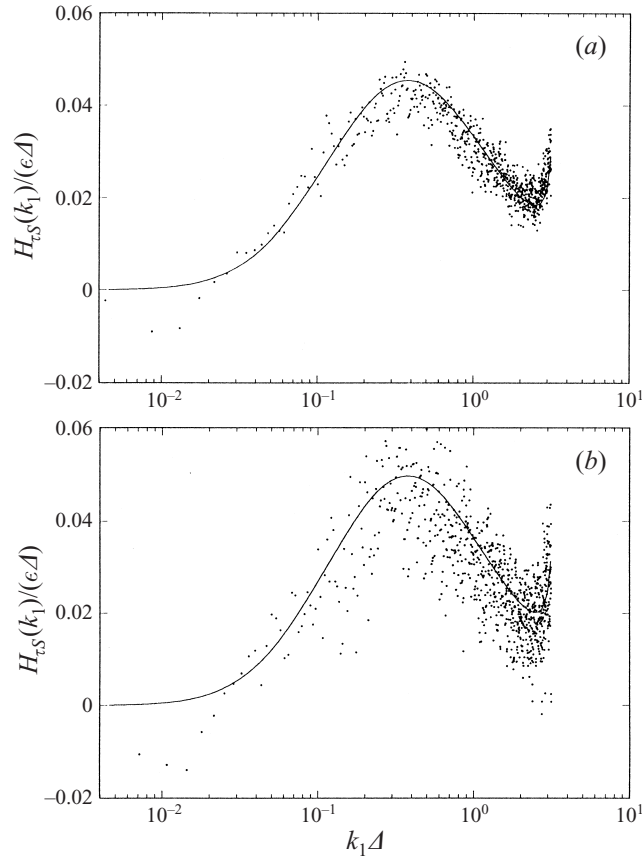
FIGURE 7. Longitudinal co-spectrum $H_{\tau S}(k_1)$ of τ_{11} and $\tilde{S}_{11}$ measured from the (*a*) 20V and (*b*) 25V data sets, using a mixed cutoff filter (spectral cutoff filter in the streamwise direction and array box filter in the cross-stream direction). A cusp near the filter wavenumber $k_1 = k_\Delta$ is clearly visible. The solid lines are the proposed fits (equation (3.10)).

distant interactions at least along the streamwise direction in Fourier space is provided by the negative values observed for $H_{\tau S}(k_1)$ at low k_1, which is measured directly and does not rely on the assumption of local isotropy.

As outlined in §1, the first prediction of spectral eddy viscosity was made by Kraichnan (1976) for the spectral cutoff filter. His result showed an upward trend (cusp) towards the grid scale, as opposed to the downward trend observed here for the box filter. The limited number of probes in our array precludes us from approximating a spectral cutoff filter in the cross-stream (x_2) direction. However, in time (or streamwise direction, x_1) there is no difficulty in approximating a spectral cutoff filter from the current data. While of only qualitative value, we wish to explore whether a mixed filter (spectral in x_1 and box filter in x_2) displays a cusp-like trend in eddy viscosity when approaching the filter scale. Figure 7 shows the longitudinal co-spectrum for this type of filter for the 20V and 25V data sets. Also shown is a smooth fit of the form

$$H_{\tau S}^{\mathrm{fit}}(k_1)/\varepsilon\Delta = \alpha_1 \exp\left[-1.9(\log_{10}(k_1\Delta) + 0.45)^2\right] \times \left(1 - \frac{0.1}{(\log_{10}(k_1\Delta) - 0.53)}\right) \quad (3.10)$$

with $\alpha_1 = 0.041$ for the 20V set, and $\alpha_1 = 0.045$ for the 25V data set.
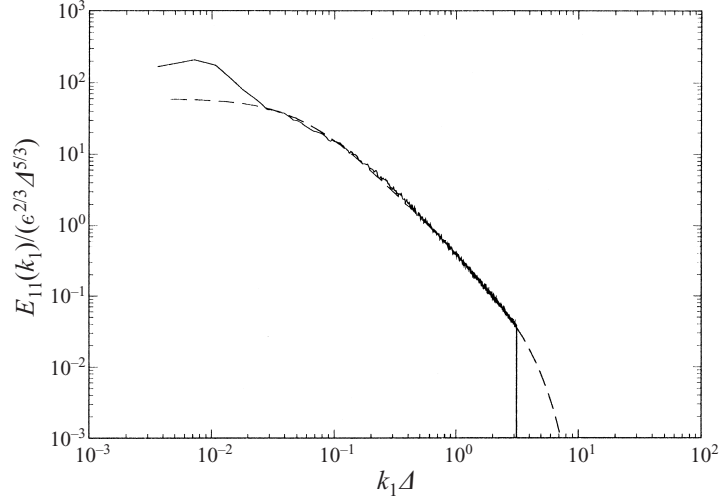
FIGURE 8. Longitudinal energy spectrum measured from the 25V data set using a mixed cutoff filter (spectral cutoff filter in the streamwise direction and array box filter in the cross-stream direction). The long-dashed line is the proposed fit (equation (3.11)).

A cusp near the grid-filter scale $k_1\Delta \sim \pi$ is clearly apparent. The energy spectrum $E_<(k_1)$ for the 25V data, processed with this mixed filter, is shown in figure 8, also including a smooth fit which in radial form is given by

$$E_<(k) = \beta_1 \varepsilon^{2/3} k^{-5/3} \left(\frac{k\ell}{\sqrt{k^2\ell^2 + \beta_2}} \right)^{11/3} e^{-\beta_3(k\Delta)^4}, \tag{3.11}$$

with $\beta_1 = 1.5$, $\beta_2 = 10$ and $\beta_3 = 5.0 \times 10^{-4}$. The fit is constructed, as before, by transforming equation (3.11) to longitudinal axes and comparing it with the measured spectrum of filtered velocity. The spectral eddy viscosity is evaluated by transforming equation (3.10) according to equation (3.7), and dividing the result by $2k^2 E_<(k)$. Results are shown in figure 9. As is evident, and consistent with the upward cusp behaviour of the measured co-spectrum, the spectral eddy viscosity has a sharp increase immediately before the grid scale. As a comparison, the fit to the EDQNM prediction of equation (1.7) is shown as a dot-dashed line, where the recommended value $a_1 = 0.441$ is used, and our measured value $\beta_1 = 1.5$ is used for C_K. As in the case of the Gaussian filter, we also show this expression after rescaling so that it integrates to the measured SGS dissipation (long-dashed curve). As can be seen, both theoretical and experimental results display a cusp behaviour, although the latter is narrower. The sensitivity to parameters (not shown) is similar to the case of the Gaussian filter (figure 6b).

As opposed to the predictions of the two-point closures, the measured $v_{re}(k, k_\Delta)$ decreases from its peak value in the inertial range before rising again in the cusp. Considering that none of the analyses of DNS (Domaradski et al. 1987; Langford & Moser 1999) and LES results (Métais & Lesieur 1992) show such an intermediate dip in spectral eddy viscosity, it is quite possible that it is caused by the mixed filter (a box filter in the cross-stream direction) employed in the experiments. On the other hand, the plateau from EDQNM (0.064, or 0.05 after rescaling) is quite consistent with the experimental results which range between 0.05 and 0.1.
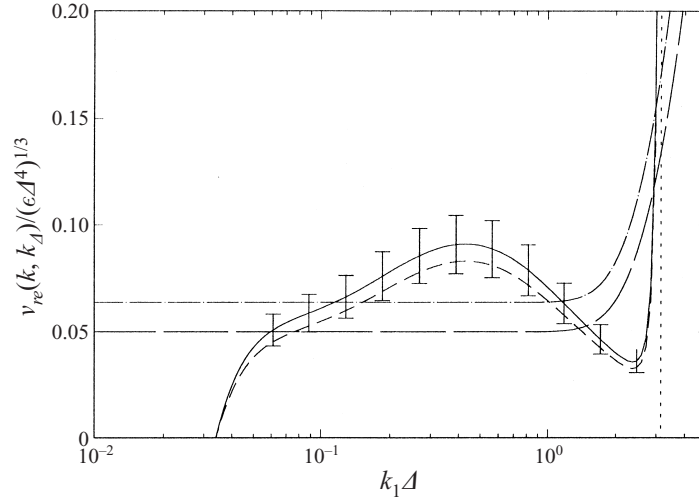
FIGURE 9. Spectral eddy-viscosity distribution measured from the 25V (solid line) and 20V (short dashed line) data sets using a mixed cutoff filter (spectral cutoff filter in the streamwise direction and array box filter in the cross-stream direction). Error bars (shown only for the 25V case) reflect the expected $\pm 15\%$ error level associated with calibration uncertainty (the same level also applies to the 20V data set). The results are normalized with $\epsilon^{1/3}\Delta^{4/3}$. The dash-dotted line is the EDQNM prediction, the long-dashed line the same prediction multiplied by 0.78 (so that the integral $\int_0^{\pi/\Delta} 2\nu k^2 E_< \, dk$ equals the measured SGS dissipation). The vertical dotted line is the cutoff filter wavenumber. The level of sensitivity to parameters (not shown) is similar to that in figure 4(*d*).

Finally, we point out that the measured distributions of spectral eddy viscosity correspond to the 'net' viscosity which, as summarized in §1, include both forward dissipation and a negative backscatter term, $U(k)$, according to the predictions of two-point closures (Kraichnan 1976; Leslie & Quarini 1979). While such a decomposition arises naturally in the closures, and is easy to implement in spectral simulations of homogeneous turbulence (Chasnov 1991), it is not clear how to perform such a decomposition on the experimental data. Decompositions into a deterministic and stochastic part – along the lines proposed by Langford & Moser (1999) or Farge, Schneider & Kevlahan (1999) – provide a promising framework, but they are not equivalent to the decomposition that arises from the closures. For instance, it is unlikely that the deterministic part would correspond to the eddy-viscosity term and that the stochastic part would account for only backscatter. Also, the other definition of backscatter commonly used in physical space (when $-\tau_{ij}\tilde{S}_{ij} < 0$ locally, see e.g. Piomelli *et al.* 1991; Liu *et al.* 1994) appears to bear little relation to the spectral backscatter term $U(k)$ that arises in the closures.

We now turn to hyper viscosity and its relationship to SGS dissipation of enstrophy and spectral eddy viscosity.

4. Hyper viscosity and SGS dissipation of resolved enstrophy

As outlined in §1, in order to reproduce a wavenumber-dependent eddy viscosity in physical space, higher-order Laplacians, or hyper viscosity may be used. In general, hyper-viscosity terms, of the form $(-1)^{n+1}\nu_n(\nabla^2)^n\tilde{u}$ in the momentum equation, can be of arbitrary order n. However, motivated by analogy to SGS energy dissipation for the Smagorinsky model ($n = 1$), we show in §4.1 that $n = 2$ arises naturally

from consideration of SGS dissipation of resolved enstrophy. Hence, we focus on the case $n = 2$, but without necessarily ruling out other values. Assuming local isotropy, the coefficient of the hyper-viscosity term is related to the derivative skewness in §4.2. Measurements of derivative skewness and implications for model parameters are presented in §4.3.

4.1. Enstrophy equilibrium condition

The basic methodology to be employed is motivated by Lilly's (1967) classic analysis of the Smagorinsky model in isotropic turbulence. There, the evolution of the mean turbulent kinetic energy is examined, either large-scale fluctuating kinetic energy $K = \frac{1}{2}(\langle \tilde{u}_i^2 \rangle - \langle \tilde{u}_i \rangle^2)$, or small-scale (subgrid) energy $k = \frac{1}{2}(\langle u_i^2 \rangle - \langle \tilde{u}_i^2 \rangle)$. Assuming homogeneous and steady-state statistics, a large Reynolds number, and a filter scale well within the inertial range, equilibrium is obtained between energy injection (equal to ϵ, the mean molecular dissipation under conditions of equilibrium) and SGS dissipation of resolved kinetic energy,

$$\epsilon = -\langle \tau_{ij} \tilde{S}_{ij} \rangle. \tag{4.1}$$

Since $\epsilon > 0$, the tensor τ_{ij} must be anti-correlated with $\tilde{S}_{ij}$. This 'empirical' fact may be used as a simple-minded justification for eddy viscosity: the simplest modelling that explicitly guarantees that such a correlation exists is to set τ_{ij} proportional to $-\tilde{S}_{ij}$. The proportionality coefficient is twice the eddy viscosity. To evaluate the coefficient c_s, Lilly proposed to use the requirement that $\tilde{u}_i$ follow the Kolmogorov spectrum down to k_Δ. This condition allows the evaluation of $\langle \tilde{S}_{ij} \tilde{S}_{ij} \rangle$ in terms of ϵ, Δ, and c_K. Coupled with the resolved energy equilibrium condition (equation (4.1)), this yields a relationship between c_s and the (empirically known) universal Kolmogorov constant c_K, namely $c_s^2 \approx \pi^{-2}(\frac{3}{2}c_K)^{-3/2}$.

We extend this approach to the resolved enstrophy field defined as $\mathscr{X} = \frac{1}{2}\tilde{\omega}_i^2$, where $\tilde{\omega}_i$ is the filtered vorticity field (Mansfield, Knio & Meneveau 1998). We begin with the transport equation for the filtered vorticity field (the *curl* of the filtered Navier–Stokes equation):

$$\frac{\partial \tilde{\omega}_i}{\partial t} + \tilde{u}_j \frac{\partial \tilde{\omega}_i}{\partial x_j} = \tilde{\omega}_j \frac{\partial \tilde{u}_i}{\partial x_j} + v \frac{\partial^2 \tilde{\omega}_i}{\partial x_j^2} - \epsilon_{ijk} \frac{\partial^2 \tau_{kl}}{\partial x_j \partial x_l} + \epsilon_{ijk} \frac{\partial f_k}{\partial x_j}. \tag{4.2}$$

Multiplying by $\tilde{\omega}_i$ and rearranging yields

$$\frac{\partial \mathscr{X}}{\partial t} + \tilde{u}_j \frac{\partial \mathscr{X}}{\partial x_j} = \tilde{\omega}_i \tilde{\omega}_j \tilde{S}_{ij} - \tau_{ij} \nabla^2 \tilde{S}_{ij} + \tilde{\omega}_i \epsilon_{ijk} \frac{\partial f_k}{\partial x_j} + \frac{\partial}{\partial x_i} Q_i - v \left(\frac{\partial \tilde{\omega}_i}{\partial x_j} \right)^2, \tag{4.3}$$

where

$$Q_i = \tilde{\omega}_j \epsilon_{ijk} \frac{\partial \tau_{lk}}{\partial x_l} - \tau_{il} \epsilon_{ljk} \frac{\partial \tilde{\omega}_k}{\partial x_j} + v \frac{\partial \mathscr{X}}{\partial x_i}$$

is the 'enstrophy flux'. We consider the case of statistically homogeneous and steady turbulence, in the limit of very large Reynolds number. Upon averaging, and assuming that the filter size Δ is well inside the inertial range where viscous and forcing effects are negligible, we obtain

$$\langle \tilde{\omega}_i \tilde{\omega}_j \tilde{S}_{ij} \rangle = \langle \tau_{ij} \nabla^2 \tilde{S}_{ij} \rangle. \tag{4.4}$$

The left-hand side represents production of resolved vorticity fluctuations, while the right-hand side represents dissipation of these fluctuations by the action of the SGS stress tensor τ_{ij}.

Since it is known that the resolved velocity field is characterized by three-dimensional vorticity fluctuations (i.e. non-zero enstrophy), there must typically be non-zero production of enstrophy, that is, $\langle \tilde{\omega}_i \tilde{\omega}_j \tilde{S}_{ij} \rangle > 0$. This implies that $\langle \tau_{ij} \nabla^2 \tilde{S}_{ij} \rangle > 0$. Enstrophy is thus dissipated by the SGS stress through its correlation with the Laplacian of the strain-rate tensor, in much the same way as energy is dissipated by the correlation of the SGS stress with $-\tilde{S}_{ij}$. The required correlation can be established by setting the stress proportional to $\nabla^2 \tilde{S}_{ij}$ (i.e. $n = 2$). In order to also reproduce a non-zero constant eddy-viscosity behaviour at low wavenumbers, a standard Smagorinsky term should be added to the hyper-viscosity term, according to

$$\tau_{ij}^{mod} = -2c_1 \Delta^2 |\tilde{S}| \tilde{S}_{ij} + c_2 \Delta^4 |\tilde{S}| \nabla^2 \tilde{S}_{ij}. \tag{4.5}$$

As mentioned before, other authors have considered hyper-viscosity models, mostly of higher order. For now, we continue to examine the weaker $\nabla^2 \tilde{S}_{ij}$ form, since it is directly motivated by SGS enstrophy dissipation, equation (4.4).

It is simple to show analytically that, in the inertial range, $\tilde{S}_{ij}$ and $\nabla^2 \tilde{S}_{ij}$ are strongly correlated. Hence, it turns out that addition of a hyper-viscosity term to the Smagorinsky model does not improve (Appendix D in Cerutti 1999) the local realism of the model as measured by correlation coefficients between the real SGS stress τ_{ij} and τ_{ij}^{mod}. As with the simple eddy-viscosity model, hyper viscosity has to be understood merely in a statistical sense, and only used to generate the correct mean SGS dissipation of selected variables. Below, we continue with this restricted interpretation.

4.2. *Parameter values and filtered derivative skewness*

In order to evaluate c_1 and c_2, we replace the expression for τ_{ij}^{mod}, equation (4.5), into the equilibrium condition between production and SGS dissipation of resolved kinetic energy (equation (4.1)) and enstrophy (equation (4.4)). The result is

$$\varepsilon = 2c_1 \Delta^2 \langle |\tilde{S}| \tilde{S}_{ij}^2 \rangle - c_2 \Delta^4 \langle |\tilde{S}| \tilde{S}_{ij} \nabla^2 \tilde{S}_{ij} \rangle, \tag{4.6}$$

$$\langle \tilde{\omega}_i \tilde{\omega}_j \tilde{S}_{ij} \rangle = -2c_1 \Delta^2 \langle |\tilde{S}| \tilde{S}_{ij} \nabla^2 \tilde{S}_{ij} \rangle + c_2 \Delta^4 \langle |\tilde{S}| (\nabla^2 \tilde{S}_{ij})^2 \rangle. \tag{4.7}$$

In order to relate the moments appearing on the right-hand side to second-order moments (which can be evaluated based on the velocity spectrum) we introduce the following three coefficients,

$$\alpha \equiv \frac{\langle \partial_k \tilde{S}_{ij} \, \partial_k (\tilde{S}_{ij} \sqrt{\tilde{S}_{mn} \tilde{S}_{mn}}) \rangle}{\langle \tilde{S}_{ij} \tilde{S}_{ij} \rangle^{1/2} \langle (\partial_k \tilde{S}_{mn})^2 \rangle}, \tag{4.8}$$

$$\beta \equiv \frac{\langle (\tilde{S}_{ij} \tilde{S}_{ij})^{3/2} \rangle}{\langle \tilde{S}_{ij} \tilde{S}_{ij} \rangle^{3/2}}, \tag{4.9}$$

$$\gamma \equiv \frac{\langle (\tilde{S}_{ij} \tilde{S}_{ij})^{1/2} (\nabla^2 \tilde{S}_{mn})^2 \rangle}{\langle \tilde{S}_{ij} \tilde{S}_{ij} \rangle^{1/2} \langle (\nabla^2 \tilde{S}_{mn})^2 \rangle}. \tag{4.10}$$

On dimensional grounds, we may expect these parameters to be of order one, so they will be set to exactly one at first; their numerical values will be evaluated later from DNS data (in his analysis, Lilly (1967) set $\beta = 1$). Next, second-order moments of $\tilde{S}_{ij}$ and its gradients are expressed in terms of the isotropic radial energy spectrum

$$E(k) = c_K \varepsilon^{2/3} k^{-5/3} \tag{4.11}$$

where c_K is the Kolmogorov constant. This constant typically ranges between 1.6 and

2.1, with low values characteristic of experimental data, and DNS yielding higher values. We will explore the effect of this range of c_K values on our results. Using isotropy, the enstrophy production term can be written as

$$\langle \tilde{\omega}_i \tilde{\omega}_j \tilde{S}_{ij} \rangle = -\tfrac{35}{2} \mathscr{S}_{\varDelta} \left\langle \left(\frac{\partial \tilde{u}_1}{\partial x_1} \right)^2 \right\rangle^{3/2}, \tag{4.12}$$

where $\mathscr{S}_{\varDelta}$ is the skewness coefficient of the filtered velocity derivative,

$$\mathscr{S}_{\varDelta} = \frac{\left\langle \left(\frac{\partial \tilde{u}_1}{\partial x_1} \right)^3 \right\rangle}{\left\langle \left(\frac{\partial \tilde{u}_1}{\partial x_1} \right)^2 \right\rangle^{3/2}}. \tag{4.13}$$

The two balance conditions for energy and enstrophy can be written as

$$\varepsilon = 2\sqrt{2}[c_1 \varDelta^2 \beta \langle \tilde{S}_{ij} \tilde{S}_{ij} \rangle^{3/2} + c_2 \varDelta^4 \tfrac{\alpha}{2} \langle \tilde{S}_{ij} \tilde{S}_{ij} \rangle^{1/2} \langle (\nabla \tilde{S}_{ij})^2 \rangle] \tag{4.14}$$

$$-\frac{7}{3\sqrt{15}} \mathscr{S}_{\varDelta} \langle \tilde{S}_{ij} \tilde{S}_{ij} \rangle = 2c_1 \varDelta^2 \alpha \langle (\nabla \tilde{S}_{ij})^2 \rangle + c_2 \varDelta^4 \gamma \langle (\nabla^2 \tilde{S}_{ij})^2 \rangle, \tag{4.15}$$

respectively. By expressing the second-order moments in terms of the Kolmogorov spectrum, after some algebra, we obtain the following linear system in the two unknowns c_1 and c_2:

$$\left. \begin{aligned} c_1 \beta I_f\left(\tfrac{1}{3}\right) + c_2 \tfrac{\alpha}{2} \pi^2 I_f\left(\tfrac{7}{3}\right) &= \left[2\pi^2 c_K^{3/2} \sqrt{2 I_f\left(\tfrac{1}{3}\right)} \right]^{-1}, \\ c_1 2\alpha I_f\left(\tfrac{7}{3}\right) + c_2 \gamma \pi^2 I_f\left(\tfrac{13}{3}\right) &= -\frac{7 \mathscr{S}_{\varDelta}}{3\pi^2 \sqrt{15}} I_f\left(\tfrac{1}{3}\right). \end{aligned} \right\} \tag{4.16}$$

The function $I_f(x)$ is defined by

$$I_f(x) = \int_0^{+\infty} \left| \hat{G}_{\varDelta}^f \left(\frac{\pi}{\varDelta} \mathscr{K} \right) \right|^2 \mathscr{K}^x \, \mathrm{d}\mathscr{K} \quad \left(\mathscr{K} = k \frac{\varDelta}{\pi} \right), \tag{4.17}$$

and depends on the filter type f. Symbolically, we use $f = b$, $f = g$, and $f = c$ to indicate the box, Gaussian, and spectral cutoff filters, respectively.

The present analysis cannot be completed for the box filter since $I_b(\tfrac{7}{3})$ and $I_b(\tfrac{13}{3})$ diverge (this simply means that the filtered high-order derivatives depend on the viscous dissipation range because of the box filter's slow $1/k$ decay in wavenumber). A similar difficulty was noted in Leslie & Quarini (1979), but they argue that consideration of the Gaussian filter should yield qualitatively similar results in the analysis. For the Gaussian three-dimensional filter, $G_{\varDelta}^g(\boldsymbol{k}) = \exp(-k^2 \varDelta^2/24)$, we have

$$I_g(x) = \frac{\sqrt{3} \Gamma((x+1)/2) 12^{x/2}}{\pi^{x+1}}. \tag{4.18}$$

where Γ is the regular Gamma function. We also consider the spectral cutoff filter defined as $\hat{G}_{\varDelta}^c(\boldsymbol{k}) = 1$ if $|\boldsymbol{k}| < \pi/\varDelta$, and zero otherwise. In that case

$$I_c(x) = \frac{1}{x+1}. \tag{4.19}$$

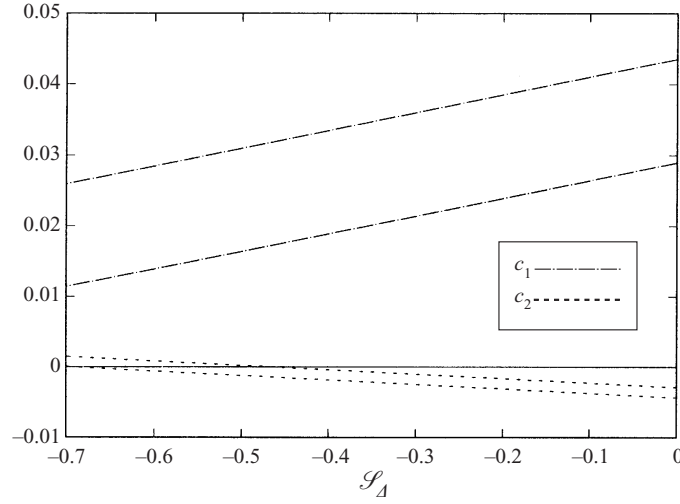As a consistency check, by setting $c_2 = 0$ in (4.16) and solving the first equation

FIGURE 10. Model coefficients c_1 and c_2 as a function of the skewness coefficient $\mathscr{S}_\Delta$, for Gaussian filter. The high c_1 line corresponds to a value of $c_K = 1.6$, the low line to $c_K = 2.1$. The low c_2 line corresponds to a value of $c_K = 1.6$, the high line to $c_K = 2.1$.

for c_1 yields

$$c_1 = \frac{1}{\beta(2I_f(\frac{1}{3})c_K)^{3/2}\pi^2} \simeq \frac{0.027}{\beta} \tag{4.20}$$

for the cutoff filter and $c_K = 1.6$. This gives the traditional value of $c_s = 0.16$ (Lilly 1967) for $\beta = 1$, with $c_1 = c_s^2$.

Returning to the system of equations for the Gaussian filter, and setting $\alpha = 1$, $\beta = 1$ and $\gamma = 1$, the solution is

$$\left.\begin{aligned} c_1 &= 0.044 + 0.025\mathscr{S}_\Delta, \\ c_2 &= -0.0044 - 0.0063\mathscr{S}_\Delta, \end{aligned}\right\} \tag{4.21}$$

for $c_K = 1.6$, or

$$\left.\begin{aligned} c_1 &= 0.029 + 0.025\mathscr{S}_\Delta, \\ c_2 &= -0.0029 - 0.0063\mathscr{S}_\Delta, \end{aligned}\right\} \tag{4.22}$$

for $c_K = 2.1$. These linear dependences are shown in figure 10.

Several features in this plot are noteworthy; when $\mathscr{S}_\Delta \simeq -0.5$, the coupled equilibrium conditions imply that $c_2 \simeq 0$, and c_1 is positive. This means that if the filtered field had the same skewness coefficient as the full velocity field (whose skewness is known to be near -0.5), the balance conditions for the Gaussian filter imply that the Smagorinsky model alone would dissipate both energy and enstrophy at approximately the correct rate. Indeed, with $c_2 = 0$, the enstrophy equation leads to

$$c_1 = -\frac{7\mathscr{S}_\Delta I_f(\frac{1}{3})}{6\alpha\pi^2 I_f(\frac{7}{3})\sqrt{15}} \simeq -0.038\frac{\mathscr{S}_\Delta}{\alpha}, \tag{4.23}$$

and to $c_s = 0.16$ if we choose $\mathscr{S}_\Delta = -0.5$ (with $\alpha = 1$). This result might suggest that the Smagorinsky model alone suffices to produce the correct enstrophy dissipation. However, this is not the case, since as will be shown based on data, $-\mathscr{S}_\Delta$ is less
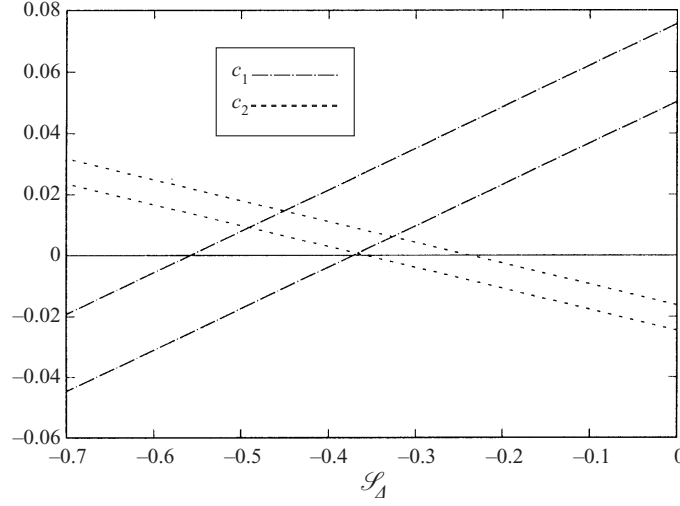
FIGURE 11. Model coefficients c_1 and c_2 as a function of the skewness coefficient $\mathscr{S}_\Delta$, for the mixed cutoff filter (a cutoff filter in the streamwise direction and box filter in the cross-stream direction). The high c_1 line corresponds to a value of $c_K = 1.6$, the low line to $c_K = 2.1$. The low c_2 line corresponds to a value of $c_K = 1.6$, the high line to $c_K = 2.1$.

than 0.5 in the inertial range. In this case, figure 10 shows that, typically, $c_2 < 0$, corresponding to a negative hyper viscosity.

For the cutoff filter and $\alpha = 1$, $\beta = 1$ and $\gamma = 1$, the solution to the system of equations (4.16) is

$$\left.\begin{aligned} c_1 &= 0.076 + 0.14\mathscr{S}_\Delta, \\ c_2 &= -0.025 - 0.069\mathscr{S}_\Delta, \end{aligned}\right\} \tag{4.24}$$

for $c_K = 1.6$, or

$$\left.\begin{aligned} c_1 &= 0.050 + 0.14\mathscr{S}_\Delta, \\ c_2 &= -0.016 - 0.069\mathscr{S}_\Delta, \end{aligned}\right\} \tag{4.25}$$

for $c_K = 2.1$. These linear dependences are shown in figure 11. Now, when $\mathscr{S}_\Delta \simeq -0.5$, the coupled equilibrium conditions imply that c_1 is close to zero, while c_2 is positive, namely that the traditional Smagorinsky term is not needed, and that the hyper-viscosity model alone could correctly dissipate both energy and enstrophy. Again, however, this is not the case since (as will be shown later) $-\mathscr{S}_\Delta$ is also less than 0.5 in the inertial range for the cutoff filter. There exists a significant range in skewness values for which both c_1 and c_2 are typically positive (about $-0.5 < \mathscr{S}_\Delta < -0.3$).

Next, we examine the spectral eddy viscosity that is implied by the mixed hyper-viscosity model. Starting from equation (4.5) for the modelled SGS stress, taking its divergence and neglecting the spatial fluctuations of $|\tilde{S}|$ (replacing $|\tilde{S}|$ with $\langle|\tilde{S}|\rangle$), the SGS term that appears in the Fourier-transformed filtered Navier–Stokes equations has the form $\nu_{\mathrm{hyp}}(k, k_\Delta)k^2\hat{\boldsymbol{u}}$, where

$$\nu_{\mathrm{hyp}}(k, k_\Delta) = \Delta^2\langle|\tilde{S}|\rangle\left[c_1 + \tfrac{1}{2}c_2(\Delta k)^2\right]. \tag{4.26}$$

Hence, $c_2 < 0$ corresponds to a downward trend of $\nu_{\mathrm{hyp}}(k, k_\Delta)$ at large k where the second term, $c_2(\Delta k)^2$, begins to dominate. Alternatively, when $c_2 > 0$, an upward (cusp-like) behaviour is obtained at high k.
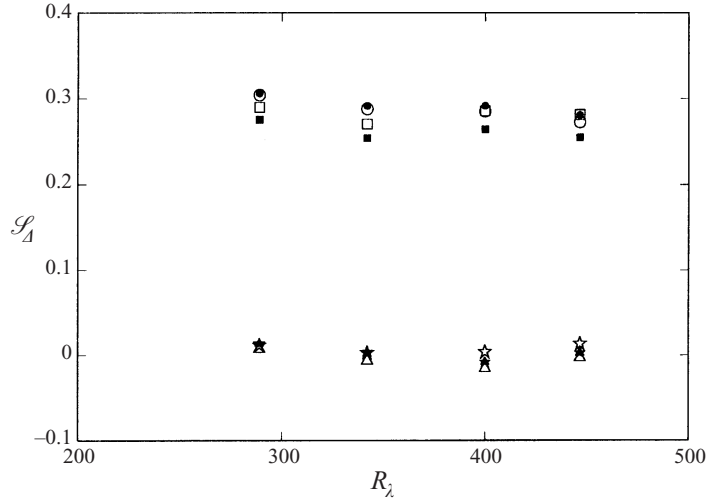
FIGURE 12. Skewness coefficient of filtered velocity derivatives evaluated from the probe array data in the cylinder wake as a function of the Reynolds number, using different graded filters. Open symbols: box filter. Closed symbols: approximated Gaussian filter. Skewness of $\partial\tilde{u}_1/\partial x_1$ (circles), of $\partial\tilde{u}_2/\partial x_2$ (squares), of $\partial\tilde{u}_1/\partial x_2$ (triangles), and of $\partial\tilde{u}_2/\partial x_1$ (stars). The experimental error level (not shown) is at $\pm 15\%$.

Recapitulating up to this point, we have shown that from simple coupled equilibrium conditions of kinetic energy and enstrophy, basic qualitative trends in spectral eddy viscosity can be predicted. Specifically, if $-\mathscr{S}_\Delta$ at high-Reynolds-number turbulence with Δ in the inertial range is below the classical value of 0.5 (but above 0.3), it turns out that these trends are in agreement with the predictions of classical two-point closures: near the filter wavenumber, the spectral eddy viscosity implied by the mixed hyper-viscous model has a downward trend for the Gaussian filter, and an upward cusp for the cutoff filter. In the next section, $\mathscr{S}_\Delta$ is measured from the data.

4.3. *Derivative skewness of filtered turbulence*

The skewness coefficients of filtered velocity derivatives, evaluated from the probe-array measurements in the cylinder wake described in §2.1, are shown in figure 12. Results are presented for the four different Reynolds numbers (data sets 10V–25V). The open symbols are for the approximate two-dimensional box filter already used in §3. Also shown in figure 12 is the skewness of $\partial\tilde{u}_2/\partial x_2$ and of the transverse gradients $\partial\tilde{u}_1/\partial x_2$ and $\partial\tilde{u}_2/\partial x_1$. The derivatives in the x_2-direction are evaluated using finite differences over a distance $\Delta/2$ based on a three-point formula for the box-filtered velocity, as in Cerutti & Meneveau (2000). It is apparent that the results are consistent with local isotropy; both longitudinal skewness coefficients are approximately equal, and the transverse skewnesses are near zero. The skewness of filtered longitudinal derivatives is near -0.3. Since the skewness is a third-order moment, we associate again a 15% error level to these experimental results (not shown in the figures).

The preceding result is, however, for the box filter, for which the analysis of §4.2 does not apply because the integrals $I_b(\frac{7}{3})$ and $I_b(\frac{13}{3})$ diverge. The analysis of the experimental data is thus repeated for an approximation of the Gaussian filter. In
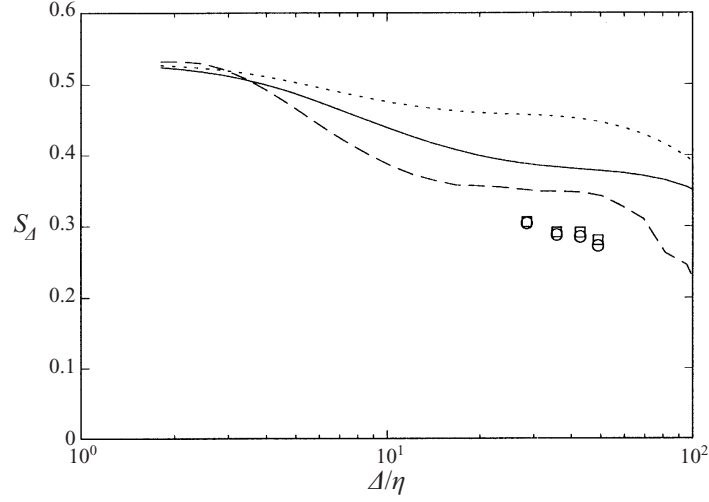
FIGURE 13. Skewness coefficient of filtered longitudinal velocity derivative $\partial \tilde{u}_1/\partial x_1$ as function of filter scale. Symbols: experimental results obtained from the probe array data in the cylinder wake at various R_λ. Lines: results from DNS at $R_\lambda \sim 150$. Solid line: Gaussian two-dimensional filter. Dotted line: Gaussian three-dimensional filter. Dashed line: three-dimensional spectral cutoff filter.

one dimension, the physical space expression for the Gaussian filter is

$$G_\Delta(x_1) = \frac{1}{\Delta}\sqrt{\frac{6}{\pi}}\exp\left(-6(x_1/\Delta)^2\right), \tag{4.27}$$

whose implementation in the streamwise direction poses no difficulties owing to the high-frequency sampling of the data. Conversely, in the cross-stream direction, only an approximation to the Gaussian filter can be applied based on the data from the probe array. Taking, as before, a filter size Δ equal to twice the inter-probe distance, the approximated cross-stream Gaussian-filtered velocity at the probe mid-point $x_2^{(O)}$ (see §2.1 for a description of probe coordinates) is given by

$$\tilde{u}_i(x_1, x_2^{(O)}) \simeq \frac{1}{2\exp(-27/8) + 2\exp(-3/8)}[\exp(-27/8)u_i(x_1, x_2^{(A)})$$

$$+ \exp(-3/8)u_i(x_1, x_2^{(B)}) + \exp(-3/8)u_i(x_1, x_2^{(C)})$$

$$+ \exp(-27/8)u_i(x_1, x_2^{(D)})]$$

$$= \frac{u_i(x_1, x_2^{(A)}) + \exp(3)u_i(x_1, x_2^{(B)}) + \exp(3)u_i(x_1, x_2^{(C)}) + u_i(x_1, x_2^{(D)})}{2 + 2\exp(3)}.$$

$$(4.28)$$

A similar formula applies to a three-point average, which is used to evaluate derivatives in the x_2-direction (Cerutti & Meneveau 2000). The solid symbols in figure 12 show the resulting skewness coefficients in the different directions. Comparison with open symbols of the box filter shows that the results are almost identical.

In figure 13, the experimental results for the skewness are plotted as a function of Δ/η. Data at different Reynolds numbers have different η, although Δ is kept constant since the same probe array is used at the different speeds.
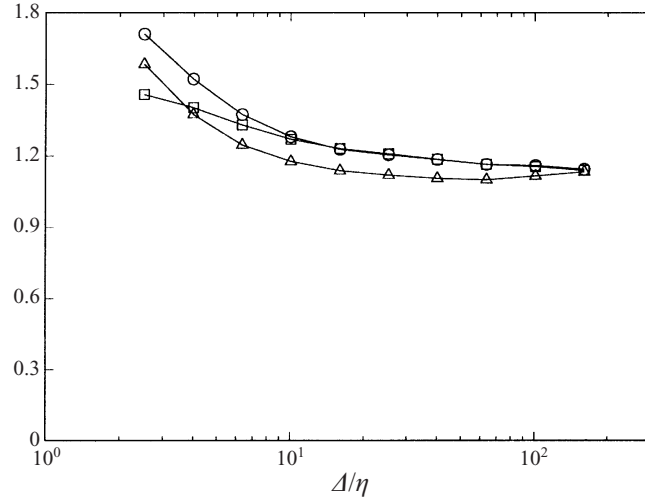
FIGURE 14. Correction coefficients α (circles), β (squares), and γ (triangles) as measured from forced DNS of isotropic turbulence on 256^3 modes at $R_\lambda \sim 150$. The filter type is a spectral cutoff filter.

We also analyse DNS of forced isotropic turbulence. The DNS (Cerutti & Meneveau 1998) uses 256^3 modes and involves constant energy injection. The Reynolds number is $R_\lambda \sim 150$. Various types of filters are applied to the DNS velocity field, including a three-dimensional and a two-dimensional Gaussian filter, and a three-dimensional spectral cutoff filter. Before reporting results for the longitudinal derivative skewness, we use the filtered DNS to evaluate the coefficients α, β and γ (defined in equations (4.8), (4.9) and (4.10)) as function of filter scale. Results plotted in figure 14 for the spectral filter show that in the inertial range ($\Delta/\eta \sim 40$) all three coefficients are near 1.2, i.e. of order one. We have checked that taking the values implied by the DNS results (e.g. $\alpha = 1.19$, $\beta = 1.19$ and $\gamma = 1.11$ for the spectral cutoff filter) does not change the results appreciably. For instance, for $c_K = 1.6$, the solution to the system of equations is

$$
\left.
\begin{aligned}
c_1 &= 0.073 + 0.14\mathscr{S}_\Delta, \\
c_2 &= -0.025 - 0.071\mathscr{S}_\Delta,
\end{aligned}
\right\} \tag{4.29}
$$

instead of equation (4.24). (Note that the coefficients increase significantly as the viscous range is approached.) The growth of β as $\Delta \to \eta$ could explain the observation in Meneveau & Lund (1997) that the Smagorinsky coefficient as determined *a priori* from DNS differs from a theoretical prediction as $\Delta \to \eta$ (see their figures 1 and 2).

Next, $\mathscr{S}_\Delta$ is computed from the filtered DNS as a function of the filter scale. The results, shown in figure 13, demonstrate that the skewness is a function of filter scale and filter type. As $\Delta/\eta \to 1$, $\mathscr{S}_\Delta$ tends to the classical value of -0.5 for unfiltered turbulence. At larger scales, $|\mathscr{S}_\Delta|$ is lower than 0.5. We also see that $-\mathscr{S}_\Delta$ for the Gaussian filter is larger than for the spectral cutoff filter, and that for the three-dimensional filter, $-\mathscr{S}_\Delta$ is larger than for the two-dimensional filter although the main trends are similar. Also, for the Gaussian filter, the experimental results are lower than those of the two-dimensional filtered DNS. These differences illustrate the sensitivity of $\mathscr{S}_\Delta$ to details of the filter type and filter scale. This sensitivity prevents us from assigning a unique value to $\mathscr{S}_\Delta$ in the inertial range. Nevertheless, taken together, the results show that $-\mathscr{S}_\Delta$ for Δ in the inertial range is smaller than 0.5, and,
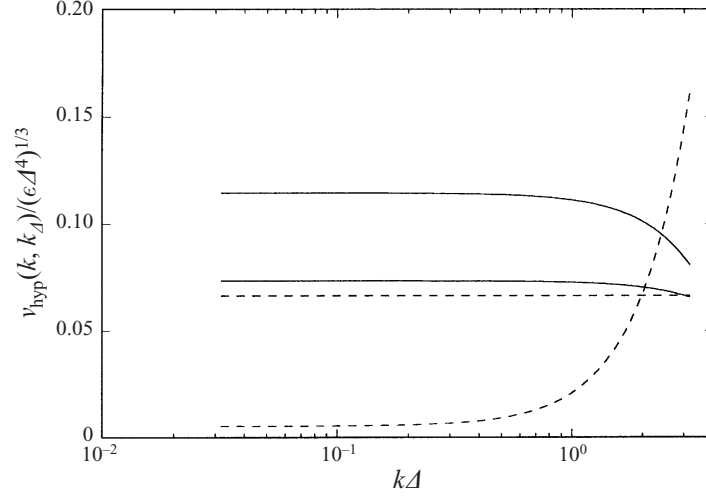
FIGURE 15. Spectral eddy viscosity of the mixed hyper-viscosity model. Different lines correspond to different cases: solid lines are for the Gaussian filter; dashed lines are for the cutoff filter (in both cases, upper line: $c_K = 1.6$, lower line: $c_K = 2.1$).

for the Gaussian filter, the results appear to fall in a broad range of $\mathscr{S}_{\Delta} \sim -0.4 \pm 0.1$, while for the cutoff filter the result is slightly lower, nearer to $\mathscr{S}_{\Delta} \sim -0.35$.

4.4. Interpretation

Examination of figures 10 and 11 with the measured values of $\mathscr{S}_{\Delta}$ leads us to conclude that $c_2 < 0$ for the Gaussian filter and $c_2 > 0$ for the cutoff filter. Hence, according to equation (4.26), the Fourier-space behaviour of the mixed hyper-viscosity model is an upward cusp near the filter scale for the cutoff filter and a decreasing trend for the graded filters. More quantitatively, we may evaluate equation (4.26) by approximating $\langle |\tilde{S}| \rangle$ by $\langle 2\tilde{S}_{ij}\tilde{S}_{ij} \rangle^{1/2}$ and evaluating this term as before using a Kolmogorov spectrum. The result is

$$\nu_{\mathrm{hyp}}(k, k_{\Delta}) = \epsilon^{1/3}\Delta^{4/3}\pi^{2/3}\sqrt{2c_K I_f(\tfrac{1}{3})}\left[c_1 + \tfrac{1}{2}c_2(\Delta k)^2\right], \qquad (4.30)$$

where $I_f(x)$ depends on the filter type and is given by equation (4.17). For the Gaussian filter, using $\mathscr{S}_{\Delta} = -0.4$, we obtain $c_1 = 0.034$ and $c_2 = -0.002$ from equations (4.21), and therefore $\nu_{\mathrm{hyp}}(k, k_{\Delta})/(\epsilon^{1/3}\Delta^{4/3}) = 3.37[0.034 - 0.001(k\Delta)^2]$ for $c_K = 1.6$. For $c_K = 2.1$ and from equation (4.22), we obtain $c_1 = 0.019$ and $c_2 = -0.0004$, and hence $\nu_{\mathrm{hyp}}(k, k_{\Delta})/(\epsilon^{1/3}\Delta^{4/3}) = 3.86[0.019 - 0.0002(k\Delta)^2]$. The two solid lines in figure 15 display these results. The relative downward trend near the filter scale is stronger in the $c_K = 1.6$ case. In comparing with figure 6, we observe that details of the two spectral eddy-viscosities differ. By construction, the hyper-viscosity model cannot reproduce both a local peak in the inertial range plateau and a decrease near the filter scale observed in the real spectral eddy viscosity of figure 6. However, it is noteworthy that the overall level of measured spectral eddy viscosities (real and hyper viscous) are comparable among themselves, as is the fact that both decrease near the filter scale.

The comparison is repeated for the spectral cutoff filter. We use $\mathscr{S}_{\Delta} = -0.35$ and obtain, from equations (4.24), that $c_1 = 0.027$ and $c_2 = 0$, and, therefore, $\nu_{\mathrm{hyp}}(k, k_{\Delta})/(\epsilon^{1/3}\Delta^{4/3}) = 3.32[0.027 + 0(k\Delta)^2]$ for $c_K = 1.6$. For $c_K = 2.1$ and from equation (4.25), we obtain $c_1 = 0.001$ and $c_2 = 0.00815$, and, hence, $\nu_{\mathrm{hyp}}(k, k_{\Delta})/(\epsilon^{1/3}\Delta^{4/3}) =$

$3.8[0.001 + 0.0041(k\Delta)^2]$. The dashed lines in figure 15 show these results. While not apparent from this plot, the total SGS dissipation implied by these different cases (i.e. the integral of $2\nu_{\text{hyp}}(k, k_\Delta)k^2 E_<(k)$) is equal among them (up to a difference consistent with the different values of c_K). An essentially flat eddy viscosity exists at $c_K = 1.6$ (recall that for the latter case, equation (4.24) gave $c_2 \approx 0$). At higher c_K-values there is an upward cusp that becomes very strong in the $c_K = 2.1$ case. Again, comparison with figure 7 shows significant differences in the details of the curves. For instance, the directly measured spectral eddy viscosity decreases before the cusp. Some of these differences could be due to the different implementations of the cutoff filter. Broadly, however, both approaches lead to a positive cusp behaviour.

It is not surprising if the details of the hyper-viscous model do not agree with the direct measurements of spectral eddy viscosity. The latter involves much more information, i.e. the full stress–strain-rate correlation function at all r, while the mixed hyper-viscous model considered here only involves two scalar quantities, kinetic energy and enstrophy (these are related to the value and curvature of the stress–strain-rate correlation function at $r = 0$). For the case of the cutoff filter, both the experimental results and EDQNM calculation yield a steeper cusp behaviour than the k^2 tail of the hyper-viscosity model studied here. Recall that Chollet & Lesieur (1981) (see also Lesieur & Métais 1996) have proposed to approximate the cusp by iterating a Laplacian operator three times. This form corresponds to a k^4 behaviour of the spectral eddy viscosity, which is closer to the observed behaviour near the cutoff wavenumber. This suggests that, at least for the spectral cutoff-filter, improved results could be obtained by considering SGS dissipation of higher-order gradients of the velocity (e.g. the palenstrophy), in addition to energy and enstrophy.

5. Conclusions

Multi-probe hot-wire measurements of wake turbulence at moderately high Reynolds numbers were analysed to determine experimentally the spectral eddy viscosity of the flow. The spectral eddy viscosity describes the rate at which energy is transferred from a particular wavenumber in the resolved range towards all scales below the filter size. The present experiments correspond to a filter scale at the lower end of the inertial range. Two approaches were employed. The more direct approach deduced the spectral eddy viscosity from measured longitudinal co-spectra of SGS stress and filtered strain rate. The other approach was based on an ansatz of hyper viscosity. While less general than the direct approach, it was shown that the latter could be motivated from considering the expressions for SGS dissipation of enstrophy of filtered turbulence. The observed trends were that for the spatially local filters, such as the box or Gaussian filters, the spectral eddy viscosity decreases as the filter scale is approached. For the spectrally sharp cutoff filter, there was evidence of an upward cusp near the filter scale. The main qualitative difference between the predictions of two-point closures and experiments was for the cutoff filter, in which case the measured spectral eddy viscosity decreases before rising in the cusp at high wavenumbers. However, given the fact that the experimental filter was not a spectral cutoff filter in all directions, the discrepancy does not invalidate the theoretical predictions. We believe that, combined, the empirical results support the general trends predicted by the classical two-point closures (Kraichnan 1976; Leslie & Quarini 1979; Chollet & Lesieur 1981), now at Reynolds numbers significantly higher than achievable in earlier tests using DNS.

After having established the feasibility of experimental measurements of spectral

eddy viscosity in turbulence, a number of other questions could now be addressed. For instance, it would be interesting to measure the spectral eddy-viscosity properties of various models, such as the similarity and nonlinear mixed models. Other recently proposed closures such as the velocity estimation model (Domaradski & Saiki 1997), the fractal model (Scotti & Meneveau 1999) and the vortex model (Misra & Pullin 1997) can also be tested in terms of their ability to reproduce the measured spectral eddy viscosity. Finally, the technique of approximating a filter using an array of point sensors can be applied to flows at much higher Reynolds numbers. As shown in Porté-Agel *et al.* (2000*a*, *b*) and Tong *et al.* 1999, arrays of sonic anemometers can be used in atmospheric flows to measure subgrid fluxes and filtered velocity gradients. Such data could be used to evaluate stress and strain-rate co-spectra and gradient skewness coefficients to deduce the spectral distribution of eddy viscosity in very high-Reynolds-number turbulence.

REFERENCES

AKHAVAN, R., ANSARI, A., KANG, S. & MANGIAVACCHI, N. 2000 Subgrid-scale interactions in a numerically simulated planar turbulent jet and implications for modelling. *J. Fluid Mech.* **408**, 83–120.

BARDINA, J. 1983 Improved turbulence models based on large eddy simulation of homogeneous, incompressible, turbulent flows. PhD thesis, Rep. TF-19, Mechanical Engineering, Stanford University.

BARDINA, J., FERZIGER, J. & REYNOLDS, W. 1980 Improved subgrid scale models for large eddy simulation. *AIAA Paper* 80-1357.

BASTIAANS, R., RINDT, C. & VAN STEENHOVEN, A. 1998 Experimental analysis of a confined transitional plume with respect to subgrid-scale modelling. *Intl J. Heat Mass Transfer* **41**, 3989–4007.

BATCHELOR, G. 1953 *The Theory of Homogeneous Turbulence*. Cambridge University Press.

BORUE, V. & ORSZAG, S. 1995 Numerical study of three-dimensional Kolmogorov flow at high Reynolds numbers. *J. Fluid Mech.* **306**, 293–324.

BORUE, V. & ORSZAG, S. 1998 Local energy flux and subgrid-scale statistics in three-dimensional turbulence. *J. Fluid Mech.* **366**, 1–31.

BRISCOLINI, M. & SANTANGELO, P. 1994 The non-Gaussian statistics of the velocity field in low-resolution large-eddy simulations of homogeneous turbulence. *J. Fluid Mech.* **270**, 199–217.

CERUTTI, S. 1999 Statistics of filtered turbulence: experiments and simulations. PhD thesis, Johns Hopkins University.

CERUTTI, S. & MENEVEAU, C. 1998 Intermittency and relative scaling of the subgrid dissipation rate in turbulence. *Phys. Fluids* **10**, 928–937.

CERUTTI, S. & MENEVEAU, C. 2000 Statistics of filtered turbulence in grid and wake turbulence. *Phys. Fluids*, **12**, 1143–1165.

CHASNOV, J. 1991 Simulation of the Kolmogorov inertial subrange using an improved subgrid model. *Phys. Fluids* A **3**, 188–200.

CHOLLET, J. 1985 Two point closure used for a sub-grid scale model in LES. In *Turbulent Shear Flows 4* (ed. J. L. Bradbury, F. Durst, B. Launder, F. Schmidt & J. Whitelaw), pp. 62–72. Springer.

CHOLLET, J. & LESIEUR, M. 1981 Parametrization of small scales of three-dimensional isotropic turbulence utilizing spectral closures. *J. Atmos. Sci.* **38**, 2747–2757.

CLARK, R. A., FERZIGER, J. H. & REYNOLDS, W. C. 1979 Evaluation of subgrid models using an accurately simulated turbulent flow. *J. Fluid Mech.* **91**, 1–16.

DANTINEE, G., JEANMART, H., WINCKELMANS, G. & LEGAT, V. 1998 Hyperviscosity and vorticity-based models for subgrid scale modeling. *Appl. Sci. Res.* **59**, 409–420.

DOMARADSKI, J., METCALFE, R., ROGALLO, R. & RILEY, J. 1987 Analysis of subgrid-scale eddy viscosity with use of results from direct numerical simulation. *Phys. Rev. Lett.* **58**, 547–550.

DOMARADSKI, J. & SAIKI, E. 1997 A subgrid-scale model based on the estimation of unresolved scales of turbulence. *Phys. Fluids* **9**, 1–17.

FARGE, M., SCHNEIDER, K. & KEVLAHAN, N. 1999 Nongaussianity and coherent vortex simulations for two-dimensional turbulence using an adaptive orthogonal wavelet basis. *Phys. Fluids* **11**, 2187–2201.

GERMANO, M., PIOMELLI, U., MOIN, P. & CABOT, W. H. 1991 A dynamic subgrid-scale eddy viscosity model. *Phys. Fluids* A **3**, 1760–1765.

HERRING, J. 1979 Sub-grid scale modeling – introduction and overview. *Turbulent Shear Flows I*, pp. 347–352. Springer.

HERRING, J. 1990 Comparison of closure to spectral-based large eddy simulations. *Phys. Fluids* A **2**, 979–983.

KALTENBACH, H. 1997 Cell aspect ratio dependence of anisotropy measures for resolved and sub-grid scale stresses. *J. Comput. Phys.* **136**, 399–410.

KRAICHNAN, R. 1976 Eddy viscosity in two and three dimensions. *J. Atmos. Sci.* **33**, 1521–1536.

LANGFORD, J. & MOSER, R. 1999 Optimal LES formulations for isotropic turbulence. *J. Fluid Mech.* **398**, 321.

LEITH, C. 1990 Stochastic backscatter in a subgrid-scale model: Plane shear mixing layer. *Phys. Fluids* A **2**, 297–299.

LESIEUR, M. & MÉTAIS, O. 1996 New trends in large-eddy simulations of turbulence. *Ann. Rev. Fluid Mech.* **28**, 45–82.

LESLIE, D. & QUARINI, G. 1979 The application of turbulence theory to the formulation of subgrid modelling procedures. *J. Fluid Mech.* **91**, 65–91.

LILLY, D. 1967 The representation of small-scale turbulence in numerical simulation experiments. In *Proc. IBM Scientific Computing Symp. on Environmental Sciences*, p. 195.

LILLY, D. K. 1992 A proposed modification of the Germano subgrid-scale closure method. *Phys. Fluids.* A **4**, 633–635.

LINDBORG, E. 1999 Correction to the four-fifths law due to variations of the dissipation. *Phys. Fluids* **11**, 510–512.

LIU, S., KATZ, J. & MENEVEAU, C. 1999 Evolution and modelling of subgrid scales during rapid straining of turbulence. *J. Fluid Mech.* **387**, 281–320.

LIU, S., MENEVEAU, C. & KATZ, J. 1994 On the properties of similarity subgrid-scale models as deduced from measurements in a turbulent jet. *J. Fluid Mech.* **275**, 83–119.

LIU, S., MENEVEAU, C. & KATZ, J. 1995 Experimental study of similarity subgrid-scale models of turbulence in the far-field of a jet. *Appl. Sci. Res.* **54**, 177–190.

MCCOMB, W. 1990 *The Physics of Fluid Turbulence*. Oxford Science.

MANSFIELD, J., KNIO, O. & MENEVEAU, C. 1998 A dynamic LES scheme for the vorticity transport equation: formulation and a-priori tests. *J. Comput. Phys.* **145**, 693–730.

MASON, P. 1994 Large-eddy simulation: a critical review of the technique. *Q. J. R. Met. Soc.* **120**, 1.

MASON, P. & THOMSON, D. 1992 Stochastic backscatter in large-eddy simulations of boundary layers. *J. Fluid Mech.* **242**, 51–78.

MENEVEAU, C. 1994 Statistics of turbulence subgrid-scale stresses: Necessary conditions and experimental tests. *Phys. Fluids* A **6**, 815–833.

MENEVEAU, C. & KATZ, J. 1999 Conditional subgrid force and dissipation in locally isotropic and rapidly strained turbulence. *Phys. Fluids* **11**, 2317–2329.

MENEVEAU, C. & KATZ, J. 2000 Scale-invariance and turbulence models for large-eddy-simulation. *Ann. Rev. Fluid Mech.* **32**, 1–32.

MENEVEAU, C. & LUND, T. 1997 The dynamic Smagorinsky model and scale-dependent coefficients in the viscous range of turbulence. *Phys. Fluids* **9**, 3932–3934.

MÉTAIS, O. & LESIEUR, M. 1992 Spectral large-eddy simulation of isotropic and stably stratified turbulence. *J. Fluid Mech.* **239**, 157–194.

MISRA, A. & PULLIN, D. I. 1997 A vortex-based subgrid stress model for large-eddy simulation. *Phys. Fluids* **8**, 2443–2454.

MONIN, A. & YAGLOM, A. 1971 *Statistical Fluid Mechanics*. MIT Press.

MURRAY, J. A., PIOMELLI, U. & WALLACE, J. M. 1996 Spatial and temporal filtering of experimental data for a-priori studies of subgrid-scale stresses. *Phys. Fluids* **8**, 1978–1980.

O'NEIL, J. & MENEVEAU, C. 1997 Subgrid-scale stresses and their modelling in the turbulent plane wake. *J. Fluid Mech.* **349**, 253–293.

OSTER, D. & WYGNANSKI, I. 1982 The forced mixing layer between two streams. *J. Fluid Mech.* **123**, 91–130.

PIOMELLI, U., CABOT, W. H., MOIN, P. & LEE, S. 1991 Sub-grid scale backscatter in turbulent and transitional flows. *Phys. Fluids* A **3**, 1766–1771.

PIOMELLI, U., YU, Y. & ADRIAN, R. 1996 Subgrid-scale energy transfer and near-wall turbulence structure. *Phys. Fluids* **8**, 215–224.

PORTÉ-AGEL, F., PARLANGE, M., MENEVEAU, C., EICHINGER, W. & PAHLOW, M. 2000*a* Subgrid-scale dissipation in the atmospheric surface layer: Effects of stability and filter dimension. *J. Hydromet.* **1**, 75–87.

PORTÉ-AGEL, F., PARLANGE, M., MENEVEAU C. & EICHINGER, W. 2000*b* A priori field study of the subgrid-scale heat fluxes and dissipation in the atmospheric surface layer. *J. Atmos. Sci.* submitted.

SARGHINI, F., PIOMELLI, U. & BALARAS, E. 1999 Scale-similar models for large-eddy simulations. *Phys. Fluids* **11**, 1596–1607.

SCHUMANN, U. 1975 Subgrid scale model for finite difference simulations of turbulent flows in plane channels and annuli. *J. Comput. Phys.* **18**, 376–404.

SCHUMANN, U. 1995 Stochastic backscatter of turbulence energy and scalar variance by random sub-grid scale fluxes. *Proc. R. Soc. Lond.* A **451**, 293–318.

SCOTTI, A. & MENEVEAU, C. 1999 A fractal model for large eddy simulation of turbulent flow. *Physica* D **127**, 198–232.

SMAGORINSKY, J. 1963 General circulation experiments with the primitive equations. I. the basic experiment. *Mon. Weather Rev.* **91**, 99.

TONG, C., WYNGAARD, J. KHANNA, S. & BRASSEUR, J. 1998 Resolvable and subgrid-scale measurements in the atmospheric surface layer: technique and issues. *J. Atmos. Sci.* **55**, 3114–3126.

TONG, C., WYNGAARD, J. & BRASSEUR, J. 1999 Experimental study of the subgrid-scale stresses in the atmospheric boundary layer. *J. Atmos. Sci.* **56**, 2277–2292.

VREMAN, B., GEURTS, B. & KUERTEN, H. 1997 Large eddy simulation of the turbulent mixing layer. *J. Fluid Mech.* **339**, 357–390.

YAKHOT, A., ORSZAG, S. & YAKHOT, V. 1989 Renormalization group formulation of large-eddy simulations. *J. Sci. Comput.* **4**, 139.

ZANG, Y., STREET, R. L. & KOSEFF, J. 1993 A dynamic mixed subgrid-scale model and its application to turbulent recirculating flows. *Phys. Fluids* A **5**, 3186–3196.